Monthly Notices of the ROYAL ASTRONOMICAL SOCIETY

MNRAS **446,** 470–492 (2015) doi:10.1093/mnras/stu2086

A deficit of ultraluminous X-ray sources in luminous infrared galaxies

W. Luangtip,[1⋆] T. P. Roberts,[1] S. Mineo,[1,2] B. D. Lehmer,[3,4] D. M. Alexander,[1] F. E. Jackson,[5] A. D. Goulding[2] and J. L. Fischer[6]

[1]*Department of Physics, University of Durham, South Road, Durham DH1 3LE, UK*
[2]*Harvard–Smithsonian Center for Astrophysics, 60 Garden Street Cambridge, MA 02138, USA*
[3]*The Johns Hopkins University, Homewood Campus, Baltimore, MD 21218, USA*
[4]*NASA Goddard Space Flight Center, Code 662, Greenbelt, MD 20771, USA*
[5]*Department of Physics and Astronomy, University of Toledo, Toledo, OH 43606, USA*
[6]*Department of Physics and Astronomy, University of Pennsylvania, 209 S. 33rd St, Philadelphia, PA 19104, USA*

Accepted 2014 October 2. Received 2014 September 17; in original form 2014 May 27

ABSTRACT

We present results from a *Chandra* study of ultraluminous X-ray sources (ULXs) in a sample of 17 nearby ($D_{\rm L} < 60$ Mpc) luminous infrared galaxies (LIRGs), selected to have star formation rates (SFRs) in excess of 7 $M_\odot$ yr^{-1} and low foreground Galactic column densities ($N_{\rm H} \lesssim 5 \times 10^{20}$ cm^{-2}). A total of 53 ULXs were detected and we confirm that this is a complete catalogue of ULXs for the LIRG sample. We examine the evolution of ULX spectra with luminosity in these galaxies by stacking the spectra of individual objects in three luminosity bins, finding a distinct change in spectral index at luminosity $\sim 2 \times 10^{39}$ erg s^{-1}. This may be a change in spectrum as 10 $M_\odot$ black holes transit from an $\sim$ Eddington to a super-Eddington accretion regime, and is supported by a plausible detection of partially ionized absorption imprinted on the spectrum of the luminous ULX ($L_{\rm X} \approx 5 \times 10^{39}$ erg s^{-1}) CXOU J024238.9-000055 in NGC 1068, consistent with the highly ionized massive wind that we would expect to see driven by a super-Eddington accretion flow. This sample shows a large deficit in the number of ULXs detected per unit SFR (0.2 versus 2 ULXs, per $M_\odot$ yr^{-1}) compared to the detection rate in nearby ($D_{\rm L} < 14.5$ Mpc) normal star-forming galaxies. This deficit also manifests itself as a lower differential X-ray luminosity function normalization for the LIRG sample than for samples of other star-forming galaxies. We show that it is unlikely that this deficit is a purely observational effect. Part of this deficit might be attributable to the high metallicity of the LIRGs impeding the production efficiency of ULXs and/or a lag between the star formation starting and the production of ULXs; however, we argue that the evidence – including very low $N_{\rm ULX}/L_{\rm FIR}$, and an even lower ULX incidence in the central regions of the LIRGs – shows that the main culprit for this deficit is likely to be the high column of gas and dust in these galaxies, that fuels the high SFR but also acts to obscure many ULXs from our view.

Key words: accretion, accretion discs – black hole physics – galaxies: starburst – infrared: galaxies – X-rays: binaries.

1 INTRODUCTION

Ultraluminous X-ray sources (ULXs; see Feng & Soria 2011 for a recent review) are extragalactic X-ray sources for which the observed luminosity in the 0.3–10 keV band reaches or exceeds the Eddington limit for an $\sim$10 $M_\odot$ black hole ($L_{\rm X} \geq 10^{39}$ erg s^{-1}). Indeed, it is now generally accepted that ULXs are accreting black holes (BHs); however, the class of BHs powering ULXs is still a topic of much debate due to their extreme luminosities. Given that they are defined as non-nuclear point-like sources, they cannot be powered by accretion on to the central supermassive black hole of their host galaxy. This then leaves two main possibilities, the first being that ULXs contain intermediate mass black holes (IMBHs, 10^2 $M_\odot \lesssim M_{\rm BH} \lesssim 10^4$ $M_\odot$), which would be accreting material at sub-Eddington rates (Colbert & Mushotzky 1999). Alternatively, ULXs could be stellar mass BHs ($M_{\rm BH} \lesssim 20\,M_\odot$) that, somehow, are accreting material at or above the Eddington rate.

In fact, although some of the very brightest ULXs remain good candidates for sub-Eddington accretion on to IMBHs, for instance

⋆E-mail: wasutep.luangtip@durham.ac.uk

HLX-1 in ESO 243-49 (Farrell et al. 2009) and a sample of extreme ULXs discussed by Sutton et al. (2012), there are many reasons to doubt this interpretation for the bulk of the ULX population. For example, it is difficult to reconcile the presence of a break in the X-ray luminosity function (XLF) of point-like X-ray sources in nearby galaxies at $\sim 1 \times 10^{40}$ erg s^{-1} (see e.g. Mineo, Gilfanov & Sunyaev 2012a) with a population of IMBHs dominating in the ULX regime. Similarly, the association of ULXs with ongoing star formation (SF, see below) is difficult to interpret solely using IMBHs (King 2004). Moreover, the high-quality X-ray spectra of multiple ULXs are inconsistent with the sub-Eddington accretion states displayed by Galactic BH binaries (Stobbart, Roberts & Wilms 2006; Roberts 2007; Bachetti et al. 2013). The spectral characteristics and high luminosities of ULXs suggest that they occupy a new, super-Eddington accretion state, named the *ultraluminous state* (Gladstone, Roberts & Done 2009; see also Sutton, Roberts & Middleton 2013b). However, some ULXs might still be massive stellar BHs (MsBHs, in the 20 $M_\odot \lesssim M_{\rm BH} \lesssim 100\ M_\odot$ regime) that could plausibly form in metal-poor environments (Zampieri & Roberts 2009; Belczynski et al. 2010; Mapelli et al. 2010), which would be accreting matter at about or slightly higher than the Eddington rate.

If stellar remnant BHs can produce such high luminosities, then there must be physical mechanisms by which they are able to accrete material at rates higher than the classical Eddington rate. Much recent theoretical work has sought to establish and/or explain these mechanisms (see e.g. Poutanen et al. 2007; Dotan & Shaviv 2011; Kawashima et al. 2012), with the notion that super-Eddington accretion rates lead to large scaleheight discs and massive outflowing, radiatively driven winds providing a plausible scenario to explain the X-ray emission characteristics. These predicted properties of super-Eddington accretion flows are now being substantiated by observations. The highest quality ULX X-ray spectra, investigated by Gladstone et al. (2009), demonstrated that ULXs appear disc-like at close to the Eddington limit (albeit the emission is broadened beyond that seen in classic disc models); at higher luminosities the spectra become two component, with a soft excess well modelled by a cool accretion disc ($kT \sim 0.2$ keV) and a harder component modelled by an optically thick corona ($kT_{\rm e} \sim 2$ keV, $\tau \sim 10$). Subsequent work has explained these spectra by attributing the cool disc component to the optically thick, massive outflowing wind that thermalizes and downscatters much of the emission within it (e.g. Kajava & Poutanen 2009; although see Miller et al. 2013), whereas the optically thick coronal component could be physically attributed to the hot inner part of the disc (e.g. Middleton et al. 2011a; Kajava et al. 2012). The broadened disc-like spectra might then be composed of the sum of these two components, emerging as the ULX begins to exceed the Eddington limit (Middleton, Sutton & Roberts 2011b). Furthermore, new work considering both spectral and timing characteristics of ULXs shows that the balance between the two components in ULX spectra appears dependent upon two factors: accretion rate and viewing angle (Sutton et al. 2013b; Middleton et al. 2014b).

ULXs are found in all types of galaxy. In elliptical galaxies there is an average $\sim$1 ULX per $10^{11}\ M_\odot$ (Feng & Soria 2011 and references therein; also Plotkin et al. 2014), a population of ULXs that must be related to the low-mass X-ray binary (LMXB) populations found in the old stellar populations of these systems. In contrast, the number of ULXs per unit stellar mass in star-forming galaxies is much higher at $\sim$1 ULX per $10^{10}\ M_\odot$, and this ratio tends to increase for the least massive galaxies (Feng & Soria 2011; also Swartz, Soria & Tennant 2008, Walton et al. 2011). This suggests that most ULXs are related to the ongoing SF hosted in younger systems, and indeed a connection between ULXs and SF is well established in the literature. For example, Fabbiano, Zezas & Murray (2001) and Gao et al. (2003) found that high numbers of ULXs were detected in individual starburst galaxies; Swartz, Tennant & Soria (2009) and Mineo et al. (2013) find a direct spatial correlation between ULXs and star-forming regions; and Mineo et al. (2012a) studied the population of high-mass X-ray binaries (HMXBs, including ULXs) in a number of star-forming galaxies via their XLFs, and found that the number of detected HMXBs is proportional to the star formation rate (SFR). In fact, the global average number of ULX detections is $\sim$2 per SFR of 1 $M_\odot$ yr^{-1} in nearby galaxies (Mapelli et al. 2010; Swartz et al. 2011). Given this relationship, we would therefore expect to detect relatively large numbers of ULXs in high-SFR galaxies, and the number of ULXs in these systems should increase proportionally with the SFR.

However, another environmental factor might also affect the production efficiency of ULXs in galaxies: metallicity. It has been suggested that ULXs should be formed in higher numbers in low-metallicity regions, as it is easier to evolve binaries to produce Roche lobe overflow on to a compact object in such environments (Linden et al. 2010). In addition, these environments should also lead to more efficient production of MsBHs via direct stellar collapse, due to reduced metal line-driven wind loss from massive stars (Zampieri & Roberts 2009; Fragos et al. 2013a,b; Mapelli & Bressan 2013). Observational support for these hypotheses is beginning to emerge. For instance, *Chandra* observations of extremely metal poor galaxies (Prestwich et al. 2013) show that the number of ULXs normalized to SFR in these galaxies is high when compared to that of metal-rich galaxies, although this is only at a formal significance of 2.3σ. Similarly, a marginally significant anticorrelation between the number of ULXs per unit SFR and metallicity was reported by Mapelli et al. (2011). In addition, Basu-Zych et al. (2013a) demonstrated that the X-ray luminosity per unit SFR of Lyman break galaxies is elevated compared to local galaxies; also a further result from a study of Lyman break galaxy analogue sample (Basu-Zych et al. 2013b) showed the anticorrelation between the X-ray luminosity per unit SFR and metallicity. They conclude that this is attributable to an enhanced population of X-ray binaries (XRBs) in the low-metallicity environment of the galaxies, that must have a very strong ULX contribution.

Given the strong relationship between ULXs and SF an obvious place to look for a large sample of ULXs is in the most active local star-forming systems. In this paper, we study the population of ULXs in such an environment – a sample of the nearest luminous infrared galaxies (LIRGs). Interestingly, such galaxies are typically relatively abundant in metals ($Z \gtrsim Z_\odot$), providing a sample of high-metallicity host environment ULXs to compare with other samples. The paper is laid out as follows. In Section 2, we describe the sample of galaxies, and how the X-ray point source catalogue for these galaxies was constructed. We detail our analyses of the ULXs, in terms of their X-ray spectra, XLF and aggregated properties in Section 3, and discuss these in light of other results in Section 4. Our findings are summarized in Section 5.

2 OBSERVATIONS AND DATA REDUCTION

2.1 Observations and initial analyses

In this paper, we study the ULX population hosted by the sample of 17 LIRGs studied in Lehmer et al. (2010), using *Chandra* X-ray observations. In brief, this sample was selected as all LIRGs within a luminosity distance ($D_{\rm L}$) of 60 Mpc with a foreground

Table 1. Properties of the LIRG sample.

Galaxy name	RA	Dec.	R_{20} ellipse parameters a (arcmin)	b (arcmin)	P.A. (deg)	D_L (Mpc)	SFR ($M_\odot$ yr^{-1})	Z	AGN?
(1)	(2)	(3)	(4)	(5)	(6)	(7)	(8)	(9)	(10)
NGC 1068	02 42 41	−00 00 48	2.42	1.99	35	13.8	7.2	9.07[1]	Y
NGC 1365	03 33 36	−36 08 25	4.60	3.45	50	18.0	9.1	9.01[1]	Y
NGC 7552	23 16 11	−42 35 05	2.21	1.30	95	21.6	9.5	9.16[2]	N
NGC 4418	12 26 55	−00 52 39	0.83	0.45	55	32.1	10.3	–	Y
NGC 4194	12 14 09	+54 31 37	0.64	0.44	170	40.7	10.9	–	Y
IC 5179	22 16 09	−36 50 37	1.48	0.56	55	47.2	13.5	8.90[3]	N
ESO 420-G013	04 13 50	−32 00 25	0.61	0.58	110	48.2	8.5	–	Y
Arp 299	11 28 30	+58 34 10	1.42	1.25	28	48.2	73.2	8.80[3]	Y
NGC 838	02 09 39	−10 08 46	0.62	0.43	95	50.8	8.5	–	N
NGC 5135	13 25 44	−29 50 01	1.75	0.86	125	52.9	14.5	8.70[3]	Y
NGC 5395	13 58 38	+37 25 28	1.53	0.80	5	54.0	11.3	–	Y
NGC 5653	14 30 10	+31 12 56	0.76	0.70	75	55.5	11.0	–	N
NGC 7771	23 51 25	+20 06 43	1.52	0.62	75	57.9	20.6	8.80[3]	Y
NGC 3221	10 22 20	+21 34 11	1.62	0.34	167	59.5	11.1	–	N
CGCG 049-057	15 13 13	+07 13 32	0.45	0.23	20	59.8	20.4	–	N
IC 860	13 15 03	+24 37 08	0.56	0.32	20	59.9	15.1	–	Y
NGC 23	00 09 53	+25 55 26	1.13	0.54	155	60.5	9.7	–	N

Notes. Basic properties of the LIRG sample, ordered by distance (based on table 1 of Lehmer et al. 2010). Column 1: common galaxy name. Columns 2 and 3: right ascension and declination, at epoch J2000, respectively. Columns 4–6: parameters of the R_{20} region for each galaxy: semimajor axis, semiminor axis and position angle, respectively. Column 7: luminosity distance. The values in columns 1–7 were given in Lehmer et al. (2010). Column 8: SFR, corrected for an AGN contribution in the calculation (see Section 3.2). Column 9: metallicity, in the form of the oxygen abundance (i.e. 12+log(O/H)). The references are: [1]Zaritsky, Kennicutt & Huchra (1994), [2]Moustakas et al. (2010) and [3]Relaño et al. (2007). Column 10: indication of whether the galaxies possess an AGN (see text for details).

Galactic column density (N_H) $< 5 \times 10^{20}$ cm^{-2}. To qualify as LIRGs, all galaxies have total infrared (IR) luminosity (8–1000 μm band; L_{IR}) $> 1 \times 10^{11}$ $L_\odot$ (where $L_\odot$ is the bolometric luminosity of the Sun), with the most luminous LIRG in the sample – Arp 299 – as bright as $\sim 8 \times 10^{11}$ $L_\odot$. These luminosities correspond to SFRs $\gtrsim 7$ $M_\odot$ yr^{-1} for each galaxy in the sample (see Section 3.2 for the calculation of SFR). The general properties of each galaxy are shown in Table 1. For the purposes of this paper, we consider all galaxies for which Lehmer et al. (2010) present evidence of possessing an AGN in their tables 1 and 3 (including the two objects classified as harbouring LINER/Sy 2 nuclei) as AGN hosts. The effect of an AGN contributing to the host galaxy IR emission and hence SFR will be taken into account in the following analyses.

The observational data for these LIRGs were extracted from the *Chandra* data archive.[1] For the few galaxies that have multiple archival data sets, we selected the observation with the longest exposure time in order to obtain the most complete snapshot of the ULX population, and the best quality data for each individual object. The exception to this was NGC 1365, for which we selected an observation with shorter exposure time as it covered a larger fraction of the galaxy's area, as defined by the R_{20} ellipse,[2] than the longest exposure, but still permitted us a statistically complete vista of the ULXs within its field of view (see Section 2.2.3). We decided not to merge the observations together to avoid an artificial boost in the number of ULXs compared to a single epoch observation, via the inclusion of multiple transient objects. Table 2 lists the observational data sets, we selected for our analysis; more details

Table 2. *Chandra* observational data.

Galaxy	Obs. ID[a]	Exp. time[b] (ks)	Refs.[c]
NGC 1068	344[d]	47.05	1,2,3,4,5,6
NGC 1365	3554[d]	13.42	7,8,9
NGC 7552	7848	5.08	10
NGC 4418	4060[d]	19.62	–
NGC 4194	7071	35.30	11,12
IC 5179	10392	11.96	–
ESO 420-G013	10393	12.42	–
Arp 299	1641	24.10	13,14,15,16
NGC 838	10394	13.79	–
NGC 5135	2187	26.41	–
NGC 5395	10395	15.65	17
NGC 5653	10396	16.52	–
NGC 7771	10397	16.71	–
NGC 3221	10398	18.96	–
CGCG 049-057	10399	19.06	–
IC 860	10400	19.15	–
NGC 23	10401	19.06	–

Notes. [a]The *Chandra* observation identifier. [b]The net exposure time after the removal of high background periods (see Section 2.1). [c]References to other analyses of the listed data sets, all of which were used by Lehmer et al. (2010). These are: (1) Smith & Wilson (2003); (2) Ptak et al. (2006); (3) Gültekin et al. (2009); (4) Swartz et al. (2004); (5) Swartz et al. (2011); (6) Peterson et al. (2006); (7) Strateva & Komossa (2009); (8) Wang et al. (2009); (9) Risaliti et al. (2005); (10) Grier et al. (2011); (11) Kaaret & Alonso-Herrero (2008); (12) Mineo et al. (2012a); (13) Huo et al. (2004); (14) Nelemans et al. (2010); (15) González-Martín et al. (2006); (16) Zezas et al. (2003); (17) Smith et al. (2012). [d]Galaxies with multiple observations; further details of these can be found in Lehmer et al. (2010).

[1] http://cxc.harvard.edu/cda/

[2] The elliptical isophote equivalent to a level of 20 mag arcsec^{-2} in the K_s band, see Lehmer et al. (2010) and references therein.

on the instrument and set-up for each observation are provided in table 2 of Lehmer et al. (2010).

The data were reduced using version 4.4 of the Chandra Interactive Analysis of Observation (CIAO)[3] tools. We first used the CHANDRA_REPRO script to create a new level 2 event file and a new bad pixel file, in order to utilize the latest calibration data. Then background flares were inspected and the exposure ranges that have a background level $>3\sigma$ above the mean level were removed by the DEFLARE script. The level 2 event files created by these steps were then used as the basis for further analysis.

2.2 The source catalogue

2.2.1 Source detection

We began by searching for the X-ray point source candidates within the R_{20} ellipse region of each galaxy, using the CIAO WAVDETECT algorithm, that applies a Mexican Hat wavelet function with radii of 1, 2, 4, 8 and 16 pixels to images created from the level 2 data. A detection threshold level of 10^{-6} was used, corresponding approximately to a false detection probability of 1 per 10^6 spatial resolution elements. In addition, for the galaxies in which a part of the R_{20} ellipse was on (or near) the CCD edge, i.e. NGC 1365, NGC 7552 and Arp 299, we also supplied an exposure map at 1.5 keV to the WAVDETECT algorithm, created using the FLUXIMAGE tool, in order to increase the accuracy of the source detection in these regions. WAVDETECT was run over data segregated into images in three separate energy bands per observation: soft (0.3–2 keV), hard (2–10 keV) and full (0.3–10 keV). Subsequently, the sources detected in each energy band were cross-correlated with source lists from the other bands, with individual objects detected in multiple bands identified using a matching radius of 3 arcsec. Each individual object was listed as one detection in the resulting combined source lists (one list per galaxy), with its position adopted from its full, soft or hard band detection, in that order of priority. There were a total of 214 candidate X-ray sources at this stage.

The ACIS EXTRACT package (Broos et al. 2010, 2012; hereafter AE[4]) was then used to finalize a catalogue composed of the most reliable point-like sources, and to characterize these objects. First, two low-significance sources – defined as detections which have AE binomial no-source probability >0.01 – were removed. After that, AE compared the source radial profile with the point spread function (PSF) for a point-like object at the source position and removed the sources that were not consistent with the PSF according to a Kolmogorov–Smirnov test (AE K–S probability <0.01, i.e. extended sources). We also picked out any remaining objects by eye that might still be extended, and used the SRCEXTENT[5] script to test whether to reject them, excluding ones shown to be extended objects. Briefly, the tool derived the elliptical Gaussian parameters which are most strongly correlated with the source image. The same algorithm was also applied to derive the elliptical Gaussian parameters for the PSF of a point-like object at the source position. Then these two apparent ellipses were tested for consistency given the image statistics, and the algorithm reported whether the source was extended within 90 per cent confidence intervals. In total, 61 extended sources ($\sim$30 per cent of all detected sources) were removed by the AE K–S test and SRCEXTENT tools. As the final step, we compared our point source catalogue with NASA/IPAC Extragalactic Database (NED)[6] and SIMBAD astronomical data base (hereafter SIMBAD),[7] and identified and removed the X-ray sources within 5 arcsec of each galaxy centre, to exclude all possible AGN contamination from the host galaxy; eight sources were removed in this way. We also used these data bases to search for foreground and/or background source contamination and four objects were identified, i.e. two stars, one QSO and one AGN, and removed. At the conclusion of these steps, we were left with the final catalogue of X-ray point sources for each galaxy, that we split into two source lists in Appendix A. Overall, 139 X-ray point sources were detected in 14 LIRGs; no point sources were detected in ESO 420-G013, CGCG 049-057 or IC 860. More than 50 per cent of the point sources were detected in the two nearest galaxies, NGC 1068 and NGC 1365, due to a combination of their proximity and exposure times yielding far greater sensitivity to faint point sources than in the other galaxies in the sample.

2.2.2 Source photometry

The net photon count rate detected from each point source was calculated in the 0.3–10 keV band by AE, using a polygonal aperture set to the 90 per cent encircled energy of the source PSF at 1.5 keV. The background level was set using an annulus around the source or, for the cases in which the source resided in densely populated regions or areas of heightened diffuse emission, we used a circular aperture located in a source-free region near to the source position, with a similar level of diffuse emission. The background area was set to be at least four times bigger than the source region and to encompass at least 100 counts. The web interface version of the Portable Interactive Multi-Mission Simulator (WEBPIMMS)[8] was applied to convert the calculated count rates into a 0.3–10 keV source flux, using an absorbed power-law continuum model. A typical value of ULX photon index (Γ) and column density ($N_{\rm H}$)[9] were used in the model: $\Gamma = 2$ and $N_{\rm H} = 1.5 \times 10^{21}$ cm^{-2} (see e.g. Swartz et al. 2004; Gladstone et al. 2009; Sutton et al. 2012). Finally, the luminosity of each source was calculated using the luminosity distance of its host galaxy. All source photometry is provided in Tables A1 and A2 in Appendix A, where we separate the detections into two lists according to whether their calculated luminosity is above or below the 0.3–10 keV luminosity threshold of 10^{39} erg s^{-1} used to demarcate a ULX.

2.2.3 ULX catalogue and completeness

The ULX candidates are tabulated in Table A1. The number of ULXs detected in each galaxy is shown in Table 3, and the position of the ULXs within their host galaxies are shown in Fig. 1. In total, 53 ULXs were detected in 13 LIRGs; no ULXs were detected in NGC 4418, ESO 420-G013, CGCG 049-057 or IC 860.

A pertinent question is whether we have detected all of the ULXs in each galaxy? To address this question, we calculated a completeness function for each galaxy following the method of Voss & Gilfanov (2006). We first created sensitivity maps in the full band (0.3–10 keV) for each galaxy, assuming source spectra with

[3] http://cxc.harvard.edu/ciao/
[4] http://www2.astro.psu.edu/xray/docs/TARA/AE.html
[5] http://cxc.harvard.edu/ciao/threads/srcextent/
[6] http://ned.ipac.caltech.edu
[7] http://simbad.u-strasbg.fr
[8] http://heasarc.nasa.gov/Tools/w3pimms.html
[9] Here, this is a combination of both foreground Galactic and additional, extragalactic column density.

Table 3. ULX detections and completeness per galaxy.

Galaxy	Number of ULXs[a]	log L_{comp}[b]	$K(L_{ULX})$[c]
NGC 1068	3 ± 0	37.53	1.00
NGC 1365	6^{+2}_{-1}	38.11	1.00
NGC 7552	2^{+3}_{-1}	38.47	1.00
NGC 4418	0 ± 0	38.31	1.00
NGC 4194	1 ± 1	38.55	1.00
IC 5179	8^{+0}_{-3}	38.88	0.98
ESO 420-G013	0 ± 0	38.87	0.96
Arp 299	8^{+1}_{-0}	38.96	0.93
NGC 838	2^{+1}_{-0}	39.01	0.89
NGC 5135	6^{+1}_{-2}	38.70	0.99
NGC 5395	4^{+1}_{-2}	38.85	1.00
NGC 5653	1 ± 1	38.90	0.95
NGC 7771	4^{+4}_{-0}	38.92	0.97
NGC 3221	6^{+0}_{-1}	38.90	0.99
CGCG 049-057	0 ± 0	38.87	1.00
IC 860	0 ± 0	38.86	1.00
NGC 23	2 ± 2	38.92	0.96
Total	53^{+16}_{-13}		

Notes. [a]The number of ULXs detected in each galaxy. The upper and lower limits were calculated from the number of sources whose 1σ luminosity upper limit lies within the ULX regime, and the number of ULXs with lower luminosity limit below the ULX regime, respectively. [b]The completeness luminosity in decimal logarithmic units, defined as the luminosity at which the completeness function, $K(L) = 0.9$. [c]The value of the completeness function at the minimum ULX luminosity of 10^{39} erg s^{-1}.

power-law continuum forms (we still used typical ULX model parameters: $\Gamma = 2$ and $N_H = 1.5 \times 10^{21}$ cm^{-2}, as this is appropriate for ULXs; cf. Gladstone et al. 2009; Sutton et al. 2012). We then computed the completeness function, $K(L)$, within the R_{20} region of each galaxy as per Voss & Gilfanov (2006), assuming that the fraction of cosmic X-ray background (CXB) sources contributing to the sample is small and can be neglected (this is justified in Section 2.2.4). Once the completeness functions were constructed, we defined the completeness luminosity (L_{comp}) as the luminosity at which the completeness function, $K(L) = 0.9$; i.e. no more than 10 per cent of point sources are missing in the detection at this luminosity. We found that all galaxies have $L_{comp} \lesssim 10^{39}$ erg s^{-1} (see the third column of Table 3). Indeed, as we are interested in the completeness of the ULX detection, we defined another parameter, $K(L_{ULX})$, as the completeness of the point source detection at minimum ULX luminosity of 10^{39} erg s^{-1} (the fourth column of Table 3). The analysis showed that the observations are sufficiently sensitive for 100 per cent of the ULXs to be detected in eight of the sample galaxies (i.e. $K(L_{ULX}) = 1$). In addition, the remainder of the galaxies are complete to the $\gtrsim$90 per cent level. Thus, we are satisfied that the ULX catalogue is complete in terms of ULX detection.

2.2.4 *Contamination from the CXB*

An issue that must always be considered when examining source populations in external galaxies is the extent to which these populations are contaminated by foreground and/or background interlopers. While the majority of foreground objects, particularly at low Galactic latitudes, are bright stars that are readily identified in optical images, at the high Galactic latitudes of the LIRG sample the predominant contamination comes from the background QSOs that constitute the CXB. Fortunately, this contamination can be taken into account statistically from the known CXB source counts.

The number of CXB sources contributing to the ULX catalogue was estimated using the $\log N$–$\log S$ relationships of Georgakakis et al. (2008). We first calculated the flux in the 0.5–10 keV band of a source at the minimum ULX luminosity of 10^{39} erg s^{-1} at the distance of each galaxy. Then WEBPIMMS was used to divide this minimum ULX flux between the 0.5–2 keV and 2–10 keV bands, the soft and hard bands used in Georgakakis et al. (2008), respectively. In this calculation, we used a CXB AGN-like power-law spectrum to convert the flux between energy bands; a Galactic column density of 5×10^{20} cm^{-2} (the upper limit on the foreground Galactic column density of the LIRGs) and a photon index of 1.7. We then converted these minimum fluxes to a maximum CXB contribution per unit area using equation 2 of Georgakakis et al. (2008), before normalizing the CXB contamination estimate to the R_{20} area of every LIRG in both the soft and hard bands. Finally, we summed these contamination estimates together to calculate a total contamination for the sample.

The calculation predicts a total of $\sim$10 soft band contaminants, and $\sim$14 contaminants in the hard band. This compares to 46 soft band detections,[10] and 27 hard band detections, leading to contamination estimates of $\sim$22 and $\sim$52 per cent, respectively. However, we regard these numbers as upper limits, for the following reasons. First, the soft band numbers do not account for the absorption of the background CXB source photons by the cold, neutral interstellar medium of the LIRGs. This will act to reduce the detectability of the background objects, and so diminish the numbers of contaminants. Secondly, the calculation is based on detectability in the full band; this does not guarantee a detection in the hard band. Indeed, in many galaxies a full band detection of a ULX is at the limit of the capabilities for the given exposure times (cf. the completeness analysis in Section 2.2.3). So, given that <30 per cent of the photons detected by the *Chandra* ACIS-S detector for the AGN-like spectral model used here are above 2 keV, these would not result in hard band detections for the ULX flux limit (although, conversely, given that most of the photon flux is below 2 keV the situation is not as bad for that band – as is indeed shown by the relative soft/hard detection statistics given above). Indeed, a factor of $\sim$4 increase in flux would be required to turn these full band detections into hard band detections; this means that the current estimate of contamination in this band is very likely a grossly inflated overestimation. We therefore disregard it, and quote only the soft band upper limit of $\lesssim$ 22 per cent contamination for the sample. We note this is relatively low (thus permitting the analysis in Section 2.2.3), so we are confident our sample is dominated by bona fide ULX detections. It is also consistent with the contamination fractions in previous similar ULX sample studies, with $\sim$15 per cent of the ULXs detected in the spiral galaxy samples of Swartz et al. (2004) and Walton et al. (2011) estimated to be background objects via similar calculations.

3 DATA ANALYSIS AND RESULTS

3.1 Spectral analyses

The selection of a large sample of ULXs permits us to perform several experiments to investigate their properties, and how these

[10] Given the low effective area of ACIS-S below 0.5 keV, we regard our 0.3–2 keV band as equivalent to the 0.5–2 keV band to first order.

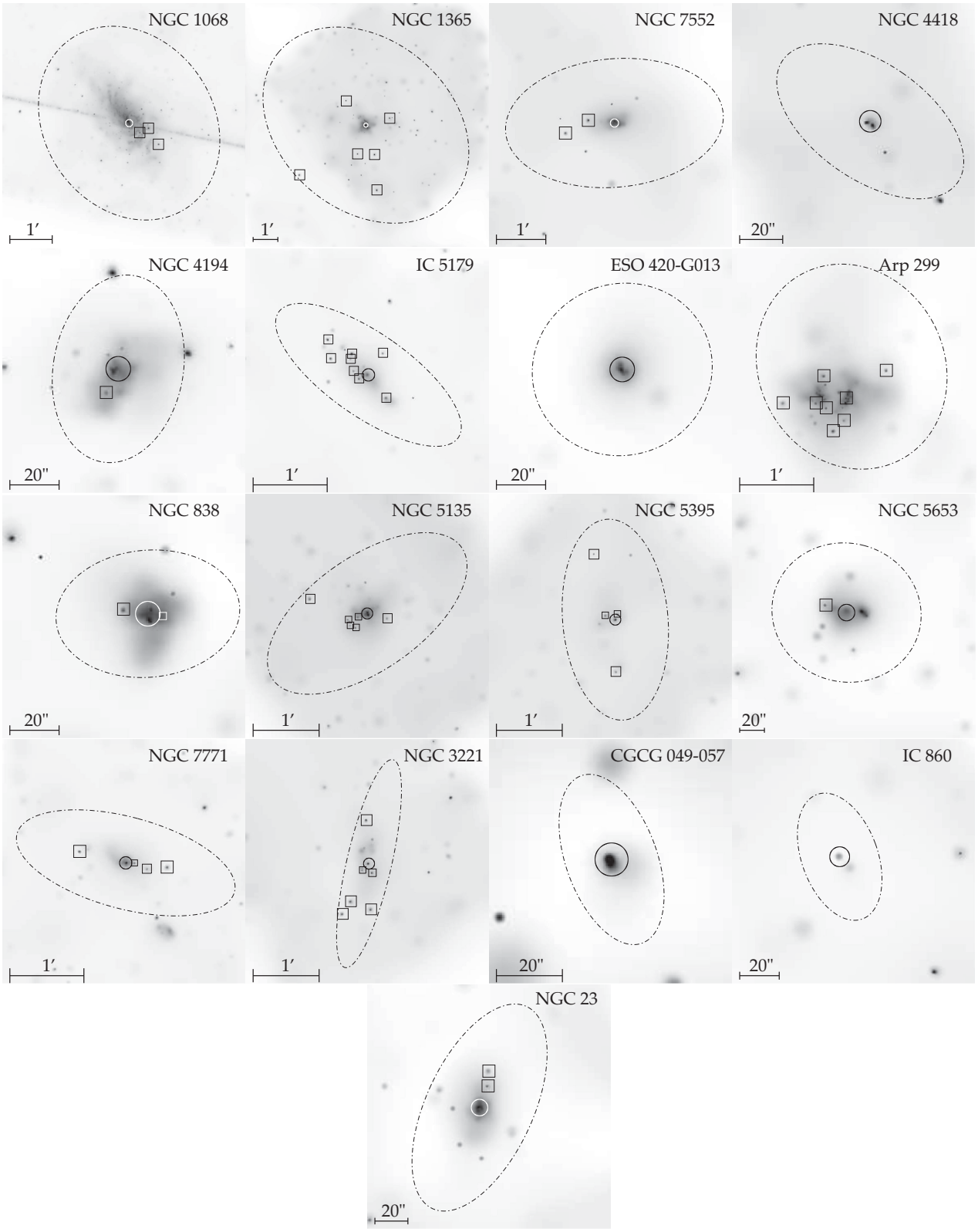

Figure 1. The ULX detections (boxes), presented on the 0.3–10 keV *Chandra* X-ray images of their host galaxies. The images were adaptively smoothed using the CSMOOTH algorithm with an S/N ratio set between 2–3 and a minimum smoothing scale of 0.5 pixels for a Gaussian kernel, and are displayed with arbitrary logarithmic scaling intended in each case to permit the ULXs to be visible. The dash–dotted ellipses define the R_{20} region of each galaxy, and the circles indicate the 5 arcsec radius regions excluded from the point source analysis due to their proximity to the nucleus. Note that no exclusion was made in the case of Arp 299 where the irregularity of this galaxy merger makes the definition of a single nuclear position difficult.

properties relate to that of their host galaxies. One such experiment is to examine how their spectra evolve as a function of luminosity, where our sample can act as an independent control to investigate the suggested evolution from the study of the nearest and brightest objects, such as presented in Gladstone et al. (2009). However, given the low number of counts available for most of the ULX detections in our sample (cf. Table A1), it is clear that we cannot do this for each individual ULX. Hence, we simply split the ULXs by luminosity, segregating into three equal logarithmical luminosity bins: low luminosity ($39 \leq \log L_{\rm X} < 39.33$, 25 sources); medium luminosity ($39.33 \leq \log L_{\rm X} < 39.67$, 21 sources) and high luminosity ($39.67 \leq \log L_{\rm X} < 40$, 6 sources), and proceeding to study their stacked spectra. These luminosity boundaries are broadly supported by evidence that ULXs do change in their spectral shape, from a disc-dominated to a two-component ultraluminous regime, at a luminosity $\sim 3 \times 10^{39}$ erg s^{-1} (cf. Gladstone et al. 2009; Sutton et al. 2013b). In one case – CXOU J024238.9-000055 – the high number of counts detected would have dominated the stacked spectrum of the high-luminosity bin, and so we study it individually below.

We extracted the spectrum of each ULX using the CIAO SPECEXTRACT script. The same source and background regions as were used to extract source photometry in Section 2.2.2 were also used here as data extraction apertures. Once extracted, the spectra were stacked by the COMBINE_SPECTRA script using the *summation* method, to create a single spectrum for each luminosity bin, and grouped to a minimum of 25 counts per bin to permit χ^2 fitting. In the case of CXOU J024238.9-000055, the individual spectrum was also grouped to a minimum of 25 counts per bin. The spectra were then fitted in XSPEC[11] version 12 over the energy range 0.3–10 keV. In the following fits, the absorption is modelled using the TBABS model with interstellar abundances set to the values of Wilms, Allen & McCray (2000); we do not explicitly account for foreground Galactic column in the fits as the stacked spectra will contain data from objects with differing values of this parameter, although we note that the initial selection criteria of the LIRG sample ($N_{\rm H} < 5 \times 10^{20}$ cm^{-2}) ensures this is relatively low. All best-fitting spectral parameter values are quoted with 90 per cent confidence intervals (Avni 1976) unless otherwise specified.

3.1.1 *Combined spectral fits*

We began by fitting the stacked spectra with a simple empirical model, namely an absorbed power-law. The results are shown in Fig. 2 and the model-fitting parameters are reported in Table 4. Two main results are apparent. First, the absorption for this model is consistent between all three luminosity groups at $\sim 2 \times 10^{21}$ cm^{-2}; this is significantly (∼four times) higher than the foreground columns for any of the LIRGs, indicating that absorption from cold material is present in these galaxies. Secondly, a significant change in the stacked spectrum is seen between the low- and medium-luminosity groups, with the spectrum hardening from $\Gamma \sim 2.3$ to ∼1.5, respectively. However, the spectrum then remains constant (within errors) between the medium and high spectra: there is no statistical distinction in power-law photon index between these two luminosity bins.

Similar results were seen when an absorbed multicolour disc blackbody model (MCD, DISKBB in XSPEC; Mitsuda et al. 1984) was used instead. In this case, the absorption columns ($N_{\rm H}$) of the three luminosity bins were also formally consistent with each other, and

[11] http://heasarc.gsfc.nasa.gov/xanadu/xspec/

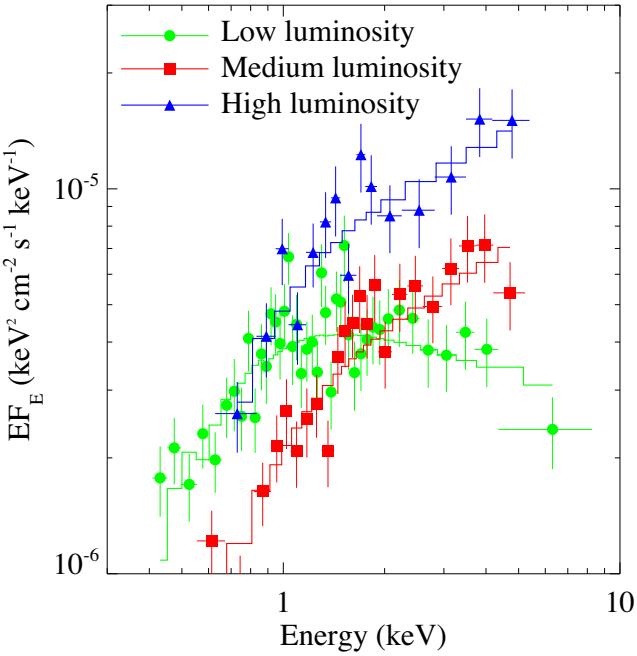

Figure 2. The stacked spectra of the low- ($39 \leq \log L_{\rm X} < 39.33$, green circle), medium- ($39.33 \leq \log L_{\rm X} < 39.67$, red square) and high- ($39.67 \leq \log L_{\rm X} < 40$, blue triangle) luminosity groups, unfolded from the detector response. We also show the best-fitting power-law continuum model as the similarly coloured solid line in each case.

with no absorption, although the column for the low-luminosity group had a much lower upper limit than the more luminous bins. But again, a significant hardening is seen between the low- and medium-luminosity bins, with the medium- and high-luminosity stacked spectra very consistent. While it would not be prudent to extract physical meaning from the results of this MCD fit given the likely wide differences in underlying spectra of the contributing sources, the similarity of the main results with the power-law fit – namely an apparent change in spectrum for objects at luminosities above and below $\sim 2 \times 10^{39}$ erg s^{-1} – points at a real change in underlying spectrum.

However, one must be extremely careful when stacking spectra not to induce any characteristics into the spectra by the choice of bins, or the relative contributions of sources to the bins. In this case, we note that all the source detections with very low total counts ($\lesssim 10$ counts) lie in the lowest luminosity bin; given the predominantly soft response of *Chandra*, this raises the concern that these objects may not be contributing many counts above 2 keV, where the ACIS-S detector sensitivity falls off, thus artificially softening the stacked spectrum in this bin. However, we note two things: first, that sources would need to be very soft not to contribute counts above 2 keV in the ACIS-S – for example, an object with 10 detected counts and an intrinsic power-law slope of $\Gamma = 2.5$ and absorption $N_{\rm H} = 5 \times 10^{20}$ cm^{-2} would contribute 1–2 counts above 2 keV. Secondly, the 12 objects with low counts only contribute ∼7 per cent of the total counts to this stacked spectrum. We confirm that this is not an issue by re-stacking the spectra in the low- and medium-luminosity bins to exclude all sources with more than 70 counts; this leaves spectra with 371 and 405 counts, respectively. The power-law continuum fits to these spectra are consistent within errors with the full stacked spectrum fits to each bin, showing the same soft/hard spectral dichotomy (low-luminosity bin:

Table 4. Combined spectral fitting.

Luminosity bin	No. of sources[a]	Power-law			MCD		
		N_H[b]	Γ[c]	χ^2/d.o.f.[d]	N_H[e]	T_{in}[f]	χ^2/d.o.f.[d]
Low ($39 \leq \log L_X < 39.33$)	25	$0.19^{+0.04}_{-0.05}$	$2.31^{+0.11}_{-0.09}$	49.84/40	<0.01	$0.84^{+0.08}_{-0.06}$	60.82/40
Medium ($39.33 \leq \log L_X < 39.67$)	21	$0.25^{+0.15}_{-0.09}$	$1.48^{+0.21}_{-0.14}$	26.6/20	<0.17	$1.59^{+0.44}_{-0.24}$	21.64/20
High ($39.67 \leq \log L_X \leq 40$)	6	$0.23^{+0.20}_{-0.12}$	$1.57^{+0.21}_{-0.22}$	13.48/12	<0.13	$1.59^{+0.63}_{-0.32}$	16.66/12

Notes. [a]the number of sources contributing to the luminosity bins. [b]Total absorption column measured from power-law model (10^{22} cm^{-2}). [c]Power-law photon index. [d]χ^2 fitting statistic, and number of degrees of freedom. [e]Total absorption column measured from MCD model (10^{22} cm^{-2}). [f]Inner-disc temperature (keV). All best-fitting parameter values are reported with 90 per cent confidence intervals.

$N_H = 0.3 \pm 0.2 \times 10^{22}$ cm^{-2}, $\Gamma = 2.1 \pm 0.4$; medium-luminosity bin: $N_H = 0.4^{+0.3}_{-0.2} \times 10^{22}$ cm^{-2}, $\Gamma = 1.4 \pm 0.4$). We therefore do not consider the low-luminosity stacked spectrum to have been artificially softened by this effect.

There is one more concern about the low-luminosity bin, though; two sources (CXOU J024238-000118 and CXOU J024240-000101, both in NGC 1068) contribute roughly one-third of the counts to the bin each. We therefore examined their spectra (that were removed from the analysis reported in the above paragraph), and found that one object appears softer than the full stacked spectrum for this bin ($N_H = 0.6 \pm 0.2 \times 10^{22}$ cm^{-2}, $\Gamma = 4.4 \pm 1.1$), and the other harder ($N_H = 0.2 \pm 0.1 \times 10^{22}$ cm^{-2}, $\Gamma = 1.6 \pm 0.3$), cf. Table 4; hence their spectra average out across the bin. Considering that the other objects in this bin have a stacked spectrum that is consistent with the full stack, we confirm that the stacked spectra reflect the average of the underlying low-luminosity ULX properties. The difference in spectra can therefore be regarded as a real effect, and we discuss it further in Section 4.1.

Finally, we attempted more complex spectral model fits, in particular an absorbed MCD plus power-law model. However, in large part due to the moderate quality of the stacked spectra (a few hundred to approximately thousand counts per bin), no statistical improvements over the single component models could be discerned.

3.1.2 CXOU J024238.9-000055

CXOU J024238.9-000055 is one of the brightest ULXs in the entire sample, at $L_X \sim 5 \times 10^{39}$ erg s^{-1}, and given its location in the nearest galaxy in the sample (NGC 1068) and the relatively high exposure for this galaxy (46.9 ks), we have accumulated sufficient counts from this object for an analysis of its spectrum. Previous work has shown it has a very hard spectrum: its power-law photon index is ∼0.8–1 (Smith & Wilson 2003; Swartz et al. 2004; Berghea et al. 2008). However, this is not due to excessive pile-up on the *Chandra* detectors; its observed count rate of ∼0.03 count s^{-1} is no more than ∼5 per cent piled-up.[12] It is not due to out-of-time events from the bright AGN in NGC 1068 either; although the source is located along the readout streak,[13] we have verified using on- and off-streak backgrounds that the spectrum is not significantly affected by this detector effect (indeed, we note that the adaptive smoothing algorithm used to create Fig. 1 greatly exaggerates this effect compared to raw data). Hence, the interpretation of the unusual hardness of this ULX is currently unclear. Here, we re-analyse the data to revisit this question.

We began by fitting the ULX spectrum with an absorbed power-law continuum model. A similar result to previous work was found: the power-law index was very hard, with $\Gamma = 0.75 \pm 0.1$ and $N_H = 0.67 \pm 0.2 \times 10^{22}$ cm^{-2}(see Table 5), and produced a statistically acceptable fit (null hypothesis probability of ∼12 per cent). However, the spectrum of this source does show residuals compared to the data, with the largest feature falling below the model level at an energy of ∼1.7 keV (cf. Fig. 3). We therefore attempted to improve the fit to the data by adding a Gaussian absorption component to the power-law model. This provided a reasonably significant improvement to the fit, with $\Delta\chi^2 = 18$ for three additional degrees of freedom for a broad absorption feature (width of ∼80 eV) at 1.68 keV. However, a single broad absorption feature at that energy is difficult to explain physically.

We therefore attempted a more physically meaningful fit to the data by modelling the residual using a partial covering, partially ionized absorption model, namely the ZXIPCF model in XSPEC, on top of an underlying power-law continuum model. This produced a very similar improvement in the fit to the single Gaussian absorption line ($\Delta\chi^2 = 15$ for three additional degrees of freedom), and also largely modelled the feature at ∼1.7 keV, using an absorber with a relatively high column of $\sim 8 \times 10^{22}$ cm^{-2} and high covering factor (>0.83) of moderately ionized material ($\log \xi = 2.2$). Notably, the addition of the partial covering, partially ionized absorber led to a change in the slope of the underlying power-law continuum, with it increasing to a more typical value for a ULX of $\Gamma \sim 1.7$. This therefore appears to be a physically plausible interpretation of the spectral data for this ULX. We summarize the analysis of CXOU J024238.9-000055 in Table 5 and Fig. 3, and discuss it further in Section 4.

3.2 The correlation between ULXs and SF in LIRGs

Whilst a relationship between the presence of ULXs and ongoing SF is undisputed, the question of whether this relationship is universal, or whether it differs subtly in different environments is an open question, with evidence starting to suggest that differences may occur due to metallicity (see Section 1). Indeed, this sample itself presents an interesting puzzle – according to Swartz et al. (2011),

[12] http://cxc.harvard.edu/csc/memos/files/Davis_pileup.pdf
[13] http://cxc.harvard.edu/ciao/why/pileup_intro.html

Table 5. Spectral fitting results for CXOU J024238.9-000055.

Single power-law model	
N_H[a]	$0.67^{+0.17}_{-0.14}$
Γ[b]	$0.75^{+0.12}_{-0.11}$
χ^2/d.o.f.	65.29/53
Power-law model with Gaussian absorption	
N_H[a]	$0.75^{+0.12}_{-0.07}$
Γ[b]	$0.88^{+0.16}_{-0.11}$
Line energy[c]	$1.68^{+0.04}_{-0.08}$
Line width[d]	$0.08^{+0.07}_{-0.04}$
χ^2/d.o.f.	47.13/50
Power-law model with partial covering absorption	
N_H[a]	$0.68^{+0.30}_{-0.19}$
Γ[b]	$1.65^{+0.77}_{-0.33}$
$N_{H,\,pa}$[e]	$7.95^{+6.08}_{-2.36}$
log ξ[f]	$2.20^{+0.18}_{-0.19}$
Covering fraction[g]	>0.83
χ^2/d.o.f.	50.27/50

Notes. A fixed Galactic column of 0.04×10^{22} cm^{-2} (the column density in the direction of NGC 1068) was added to each model. [a]Absorption column intrinsic to the ULX and/or its host galaxy (10^{22} cm^{-2}). [b]Power-law photon index. [c]Central energy of the Gaussian absorption line (keV). [d]Width of Gaussian absorption line (keV). [e]Column density of partial covering absorber (10^{22} cm^{-2}). [f]Logarithm of photo-ionization parameter $\xi = L/(nR^2)$, where L is the total luminosity, n the density of the absorber and R the distance of the material from the ionizing source. [g]Covering fraction of partial covering absorber (where 0 = totally uncovered and 1 = full covering). All best-fitting parameter values are reported with 90 per cent confidence intervals.

we should see 2 ULXs per unit SFR; yet we only see 53 ULXs in a sample of galaxies with a summed SFR of $\sim$260 $M_\odot$ yr^{-1}, i.e. 0.2 ULXs per unit SFR, a factor of 10 lower than expected.[14] It is therefore of great interest to examine the relationship between ULXs and SF in our sample in more detail, and to contrast it with other samples of galaxies.

Here, two indicators are used to examine the relationship: the blue and far-infrared (FIR) luminosities of the host galaxies (L_B and L_{FIR}). As reported by Swartz et al. (2009), ULXs tend to reside in regions that have a bluer optical colour than other parts of galaxies; and it was found that the number of ULX per unit blue luminosity is likely to be enhanced in the bluer galaxies (Smith et al. 2012), suggesting a connection between ULXs and recently formed, young stellar populations. Although the blue band luminosity is not a reliable indicator of SFR, here we derive it for direct comparison with previous work. The FIR luminosity was selected as a more accurate proxy of the SFR of the galaxies. We explain how we derived these luminosities below, and the values for each individual galaxy are given in Table 6.

[14] This is not the result of different SFR estimates – although we use a different method to calculate SFR than Swartz et al. (2011), the summed SFR for our sample calculated using both methods differs by <2 per cent.

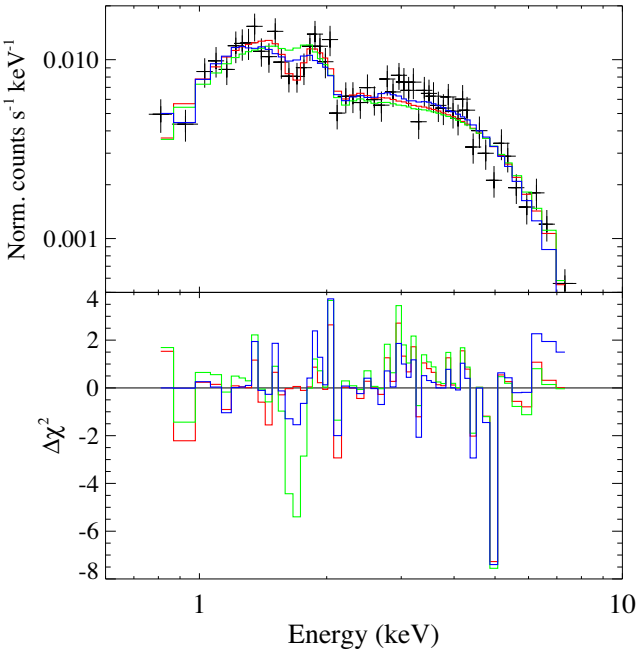

Figure 3. The spectrum of CXOU J024238.9-000055. Top panel: the spectral data (in black), with the best-fitting power-law model (green line), power-law model with Gaussian absorption component (red line) and power-law model with partial covering absorber (blue line). Bottom panel: the residual differences between the data and the best fit, with the models plotted as above.

Table 6. Blue and FIR LIRG luminosities.

Galaxy	L_B (10^{42} erg s^{-1})	L_{FIR}[a] (10^{42} erg s^{-1})
NGC 1068	26.8 ± 2.5	159.8 ± 0.3
NGC 1365	30.1 ± 1.9	201.0 ± 1.2
NGC 7552	14.2 ± 1.7	207.7 ± 4.5
NGC 4418	3.3 ± 0.0	205.9 ± 7.3
NGC 4194	10.3 ± 1.2	217.7 ± 5.3
IC 5179	33.1 ± 4.0	302.6 ± 9.5
ESO 420-G013	9.7 ± 0.0	188.0 ± 4.4
Arp 299	36.8 ± 0.0	1436.3 ± 7.2
NGC 838	8.8 ± 0.3	190.7 ± 8.7
NGC 5135	27.4 ± 3.3	318.7 ± 17.7
NGC 5395	39.8 ± 7.3	202.9 ± 8.6[b]
NGC 5653	23.1 ± 2.8	241.2 ± 12.4
NGC 7771	29.2 ± 1.3	450.4 ± 16.4
NGC 3221	24.4 ± 0.0	199.3 ± 11.1
CGCG 049-057	0.9 ± 0.0	452.5 ± 45.3
IC 860	3.1 ± 0.0	336.4 ± 33.6
NGC 23	39.3 ± 6.2	214.0 ± 12.3
TOTAL	360.4 ± 11.9	5525.2 ± 67.9

Notes. The luminosities are defined as per the text. [a]FIR luminosity, corrected for an AGN contribution to the total galaxy luminosity (see text). [b]The value may be overestimated for this galaxy because its FIR flux was not spatially resolved from its neighbouring galaxy NGC 5394.

(i) *Host galaxy blue luminosity.* Here, we define L_B to be the luminosity of the galaxy in the *B* filter of the Johnson–Morgan *UBV* system (Johnson & Morgan 1953). Most L_B values for the LIRGs were converted from *B* magnitudes corrected for extinction and redshift, which were reported in Third Reference Catalog of Bright

Galaxies (RC3 catalogue; de Vaucouleurs et al. 1991). The standard photometric value for conversion was taken from Zombeck (1990). For ESO 420-G013, we calculated L_B from the photographic B magnitude reported in the RC3 catalogue. In the case of CGCG 049-057, we took the g-magnitude from SDSS DR9[15] and then converted it to a B magnitude using the method of Windhorst et al. (1991).

(ii) *Host galaxy FIR luminosity and SFR*. As 10 out of the 17 LIRGs host AGN (see Table 1), their total FIR luminosity $L_{\rm FIR}$ (defined as their luminosity between 42.4 and 122.5 μm) will be the summation of FIR luminosity emitted from both the host galaxy and the AGN. Thus, simply using the total FIR luminosity risks overestimating the SFR of the galaxies. To correct this issue, we disentangle the FIR luminosity emitted by the AGN from the total FIR luminosity using the method of Mullaney et al. (2011). In brief, *IRAS* flux densities at four individual IR wavelengths (taken from Sanders et al. 2003) were fitted with five different host galaxy models (host galaxy IR emission templates) derived by Mullaney et al. (2011). The best-fitting models were used to predict the fraction of AGN emission contributing to the total FIR luminosity, allowing a correction to be made that left the undiluted host galaxy luminosities. Overall, the model predicted a small contribution of AGN emission to the total FIR luminosity (∼0–7 per cent), except for NGC 1068 in which the AGN emission contributes ∼27 per cent of the total FIR luminosity. The FIR luminosities of the galaxies corrected for AGN contribution are shown in Table 6.

In addition, to calculate the SFRs, we first calculated the IR luminosities in the full 8–1000 μm regime ($L_{\rm IR}$), removing AGN contamination as described above. We then used the same calibration as in Lehmer et al. (2010, their Section 2.2) to convert the total $L_{\rm IR}$ to SFR as

$$\mathrm{SFR}(\mathrm{M}_\odot\ \mathrm{yr}^{-1}) = \gamma 9.8 \times 10^{-11} L_{\rm IR}, \quad (1)$$

where $L_{\rm IR}$ is the IR luminosity in units of solar bolometric luminosity ($\mathrm{L}_\odot = 3.9 \times 10^{33}$ erg s^{-1}) and γ is the correction factor accounting for UV emission emerging from unobscured star-forming regions. The value of the latter parameter for each galaxy was estimated following the method described in section 2.2 of Lehmer et al. (2010). The SFR of each galaxy is shown in column 8 of Table 1.

3.2.1 *Global sample properties*

A convenient and simple method to compare between our sample of galaxies and others is to work out the global properties, in terms of number of ULXs ($N_{\rm ULX}$) per unit luminosity in some relevant reference band. Here, we compute this quantity for the blue and FIR luminosities introduced above. In this calculation, we also separate our ULX sample into two sub-samples, those that were detected in the AGN host galaxies and those that were detected in the galaxies without AGN. This is predicated upon the assumption that AGN feedback can affect the SFR of galaxies (see Fabian 2012 and references therein).

The calculated values of the total number of ULXs per unit luminosity are shown in Table 7.[16] First, we find no statistical distinction between the number of ULXs per unit luminosity in galaxies with and without AGN – so the incidence of ULXs appears independent of the presence of an AGN. We thus ignored this distinction, and proceeded to compare the global properties of our LIRG sample to other samples of galaxies observed by *Chandra*. These include the complete sample of 'normal' galaxies within 14.5 Mpc from Swartz et al. (2011); a sample of spiral galaxies from Swartz et al. (2004); and samples of both interacting and strongly interacting systems from Smith et al. (2012). We find that the number of ULXs per unit luminosity does depend on the host galaxy type. The ratio $N_{\rm ULX}/L_B$ appears heightened in the LIRG sample; it is three times higher (at the ∼2.7σ significance level) in the full LIRG sample than the sample of normal galaxies, with smaller, marginal significance excesses also seen above the spiral (∼1.5σ) and interacting galaxy (∼1.2σ) samples. The differences in the $N_{\rm ULX}/L_{\rm FIR}$ ratio between the LIRGs and other samples are more dramatic, with the LIRGs showing significantly suppressed ULX numbers per unit luminosity, by factors ∼5–8 (all significant at a >5.6σ level). Given that both luminosities are, to first order, related to recent SF, the fact that the ratios go in different directions compared to the other galaxy samples (i.e. an excess of ULXs compared to blue luminosity; a large deficit compared to FIR) again appears puzzling. We will discuss this further in Section 4.

Table 7. Number of ULXs per unit galaxy luminosity.

Sample	$N_{\rm ULX}/L_B$[a]	$N_{\rm ULX}/L_{\rm FIR}$[b]
All LIRGs	1471^{+447}_{-364}	959^{+290}_{-236}
LIRGs (AGN)	1478^{+420}_{-284}	861^{+242}_{-162}
LIRGs (no AGN)	1459 ± 493	1161 ± 389
Normal galaxies[1]	480 ± 50	5300 ± 500
Spiral galaxies[2]	770 ± 280	6467^{+726}_{-655}
Interacting galaxies[3]	990^{+194}_{-169}	7649^{+1315}_{-1147}
Strongly interacting galaxies[4]	1978^{+660}_{-520}	–

Notes. [a]Number of ULXs per unit galaxy blue luminosity (units of 10^{-46} (erg s^{-1})$^{-1}$). [b]Number of ULXs per unit galaxy FIR luminosity (10^{-47} (erg s^{-1})$^{-1}$). These numbers are reported with a 1σ error. The comparator samples are taken from: [1]Swartz et al. (2011); [2]Swartz et al. (2004); [3, 4]Smith et al. (2012). All reference values were calculated and reported by Smith et al. (2012).

3.2.2 *Correlation between ULXs and their host galaxy luminosities*

We also investigated whether there was any relationship between $N_{\rm ULX}$ or the cumulative luminosity of the ULXs in each individual galaxy, $L_{\rm ULX}$, and the luminosity of that galaxy in both blue and FIR light. We show scatterplots for all four possible relationships in Fig. 4, with the best-fitting linear relationship shown. Clearly, a possible relationship exists between L_B and both $N_{\rm ULX}$ and $L_{\rm ULX}$, albeit with large scatter; however, the ULX population appears not to scale with $L_{\rm FIR}$. We tested this statistically using the Pearson correlation coefficient (r), and find evidence of a positive correlation for both $N_{\rm ULX}$ and $L_{\rm ULX}$ with L_B ($r = 0.74$ and 0.65, respectively – corresponding to significance level of $\gtrsim$99.5 per cent); however,

[15] http://skyserver.sdss3.org/dr9/

[16] As Arp 299 contributes a significant fraction of the total $L_{\rm FIR}$ (∼26 per cent), we have re-calculated these values after excluding this galaxy. We find that the values in Table 7 do not change significantly, so Arp 299 does not significantly bias our results.

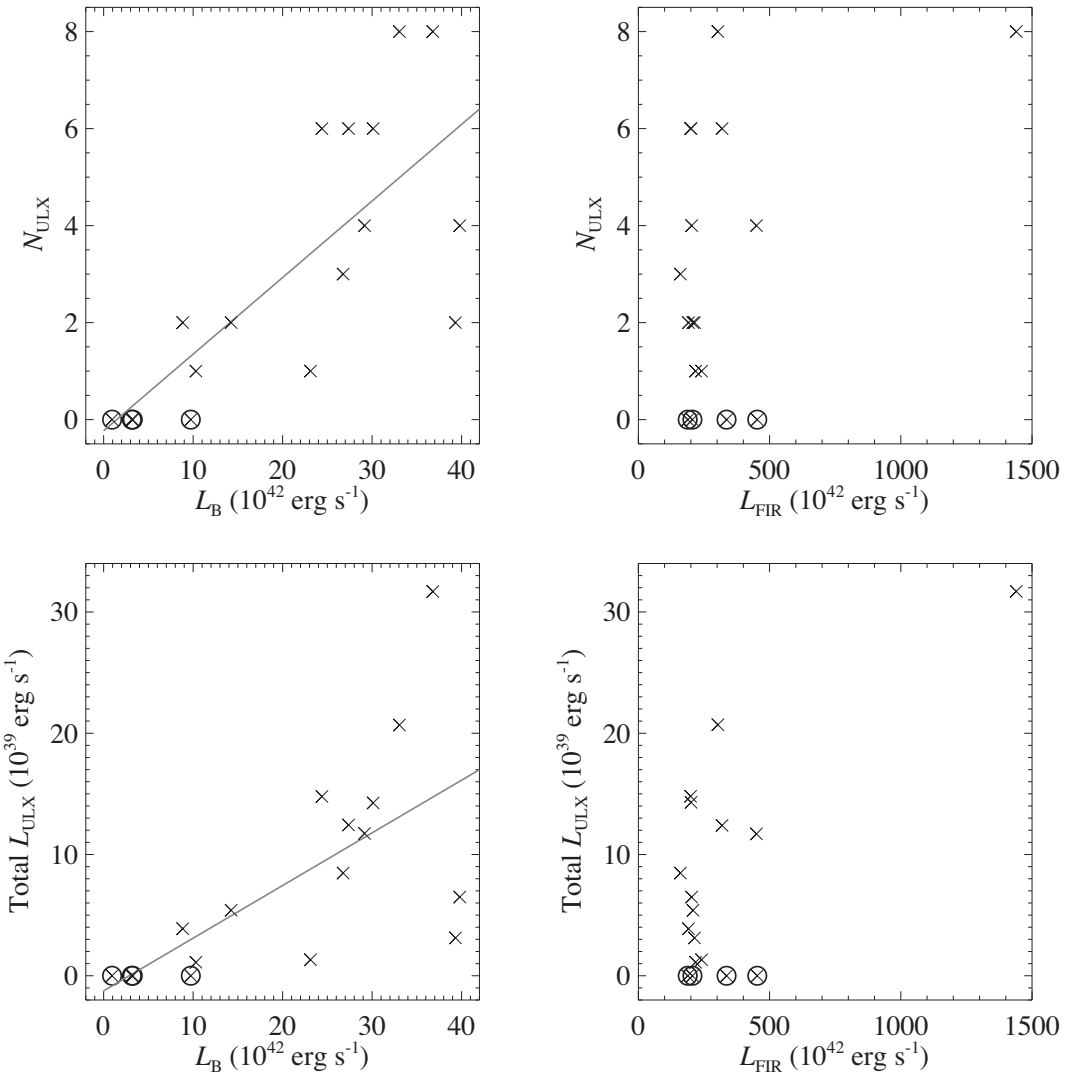

Figure 4. Scatterplots showing the ULX population properties against the host galaxy luminosities for the LIRG sample. The panels show: top left – number of detected ULXs versus host galaxy blue luminosity; top right – number of detected ULXs versus host galaxy FIR luminosity; bottom left – summed ULX luminosity versus host galaxy blue luminosity; bottom right – summed ULX luminosity versus host galaxy FIR luminosity. The linear best fit is also shown as a solid straight line in the plots in which we found a correlation (see text). The circles highlight the four galaxies in which no ULXs were detected: NGC 4418, ESO 420-G013, CGCG 049-057 and IC 860.

no evidence for a linear relationship is forthcoming for the possible relationships with L_{FIR} ($r \sim 0$ in both cases).[17]

3.3 X-ray luminosity functions

A further means of examining the ULX population of the LIRGs is by constructing their XLF. We constructed the XLF in both cumulative and differential form for the full sample of 53 ULXs, combining the data for all galaxies.

To obtain the XLF in differential form, we binned the sources into logarithmically spaced luminosity bins, taking into account the correction for incompleteness. Since we use only sources with luminosity above 10^{39} erg s^{-1}, the latter correction is small (see Table 3). We subtracted the expected contribution of background AGNs from each bin, using the log N–log S from Georgakakis et al. (2008), based on the sum of the areas within the R_{20} of all the LIRGs.[18] The number of background AGNs in each luminosity bin was computed after having converted the luminosity at the distance of each galaxy into flux. The resulting incompleteness-corrected, AGN-subtracted number of sources was normalized by the sum of the SFR of all the LIRGs.[18] The differential XLF is

[17] We confirmed that the result was not biased by the selected range of IR luminosity we used by examining the relationship between the N_{ULX}, L_{ULX} and IR luminosity in the full band (8–1000 μm). The same result was found: no correlation between N_{ULX}, L_{ULX} and the IR luminosity.

[18] Due to the fact that different galaxies have different point-source detection sensitivity, only galaxies which $K(L) \geq$ decided completeness limit should contribute to the given luminosity bin (see Mineo et al. 2012a). However, since the LIRG sample has $L_{comp} \lesssim 10^{39}$ erg s^{-1}, in this case all galaxy sample contribute to every given bin.

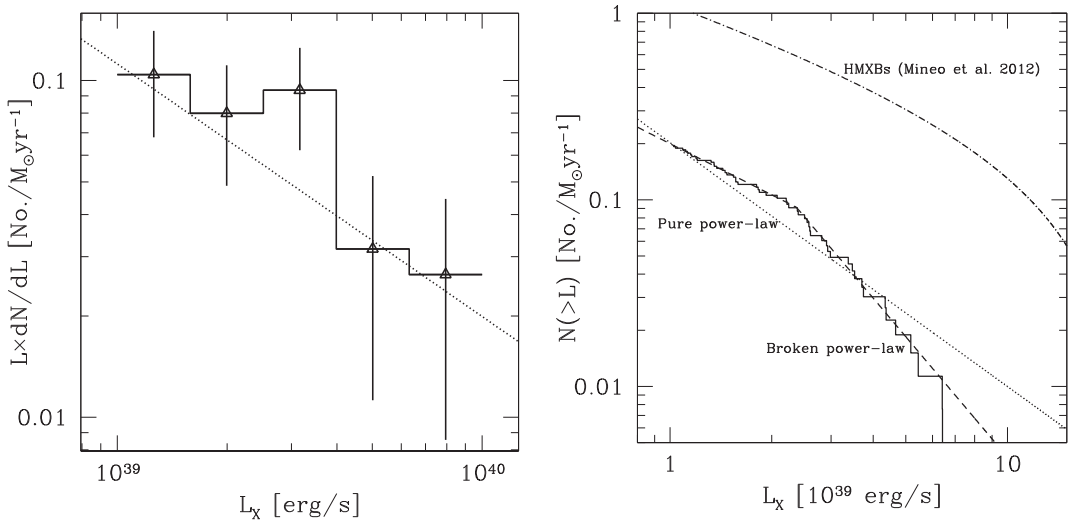

Figure 5. SFR normalized XLFs for the 53 ULXs in our sample of LIRGs. Left panel: differential XLF. We plot 1σ errors on each data point. The best-fitting pure power-law model obtained from the ML by is overlaid as a dotted line. Right panel: cumulative XLF. The best-fitting pure power-law model (similar for ML and C-stat) is plotted as a dotted line, while the broken power-law model is as a dashed line. For comparison, Mineo et al. (2012a) HMXB XLF is plotted as a dash-dotted line. All luminosities are in the 0.3–10 keV band. See Section 3.3 for details.

Table 8. XLF: fitting results from ML method.

XLF form	Pure power-law model	
	γ	A
Differential	1.75 ± 0.25	0.11 ± 0.02
Cumulative	$1.31^{+0.19}_{-0.17}$	0.20

Notes. The best-fitting results from the ML method. The definitions of the models and their parameters are given in equations (2) and (3), and the text. All best-fitting parameter values are reported with 1σ errors.

shown in the left-hand panel of Fig. 5. The error bars correspond to 1σ uncertainty using Poisson statistics and accounting for the uncertainty in the number of both ULXs and background AGNs. The combined XLF in cumulative form was constructed by integrating the unbinned differential XLF and is shown in the right-hand panel of Fig. 5. Interestingly, this highlights that there are no ULXs with luminosities above 10^{40} erg s^{-1} in our sample (see Section 4 for further discussion).

Following Mineo et al. (2012a), the fit of the XLF was performed on unbinned data using a maximum-likelihood (ML) method. The predicted contribution of resolved CXB sources was included in the model as described above. We began by fitting the XLF with a pure power-law model, defined as follows

$$\frac{\mathrm{d}N}{\mathrm{d}L_{39}} = A \times \mathrm{SFR} \times L_{39}^{-\gamma},\ L_{39} \leq L_{\mathrm{cut}}, \tag{2}$$

where $L_{39} = L_{\mathrm{X}}/10^{39}$ erg s^{-1}, $L_{\mathrm{cut}} = 10^{42}$ erg s^{-1}, A is the normalization. Using this model, we obtained the best-fitting values for the XLF parameters: $\gamma = 1.75 \pm 0.25$ and $A = 0.11 \pm 0.02$ (see Table 8). The slope is in agreement with the typical value for star-forming galaxies (Grimm, Gilfanov & Sunyaev 2003; Swartz et al. 2011; Mineo et al. 2012a). However, its normalization at 10^{39} erg s^{-1} is substantially lower than for these other XLFs, for example it is a factor of ∼5 below the normalization found by Mineo et al. (2012a).[19] This again points to a relative deficit of ULXs in the LIRG sample.

Next, We fitted the cumulative XLF with a pure power-law model (equation 2) using the ML method described above (see Table 8 for the fitting result). However, the shape of the cumulative XLF (right-hand panel of Fig. 5), induced us to search for a possible break by repeating the ML fit, using a broken power-law model:

$$\frac{\mathrm{d}N}{\mathrm{d}L_{39}} = A \times \mathrm{SFR} \times \begin{cases} L_{39}^{-\gamma_1}, & L_{39} < L_{\mathrm{b}} \\ L_{\mathrm{b}}^{\gamma_2-\gamma_1}\, L_{39}^{-\gamma_2}, & L_{\mathrm{b}} \leq L_{39} \leq L_{\mathrm{cut}}, \end{cases} \tag{3}$$

where L_{b} is the break luminosity. We did not find convergence for a break luminosity, although we explored a very broad range of parameters searching for the ML.

We repeated the fitting procedure described above using version 4.4 of the SHERPA[20] package. We first analysed the cumulative XLF. Given the unbinned nature of the cumulative data we used the CSTAT function (Cash 1979) in SHERPA to optimize the goodness of fit for the power-law model. We accounted for Poisson uncertainties on the cumulative number of sources. In this case, the broken power-law model provided an estimate for the break luminosity, $L_{\mathrm{b}} = 2.37 \times 10^{39}$ erg s^{-1}, with a substantial improvement to the fit compared to the pure power-law model (ΔC-stat of 22 for 2 additional degrees of freedom). It also appears to better describe the data by eye. However, the pure power-law model provided a statistically good fit to the data too (see Table 9), therefore we cannot reject one model in favour of the other.

The statistical significance of the break is low (∼0.5–0.8σ), which is the likely explanation for the ML procedure for a broken power-law model not converging. Moreover, none of the more

[19] Our SFR estimator assumes a Kroupa (2001) initial mass function (IMF) whereas a Salpeter IMF was used by Mineo et al. (2012a). Using this form of the IMF leads to a corrected value of the normalization of the Mineo et al. (2012a) XLF of 0.59.

[20] http://cxc.harvard.edu/sherpa4.4/

Table 9. XLF: fitting results from SHERPA.

XLF form	Pure power-law model			Broken power-law model				
	γ	A	Stat./d.o.f.[a]	γ_1	γ_2	A	L_b	Stat./d.o.f.[a]
Differential	$1.84^{+0.31}_{-0.27}$	$0.15^{+0.05}_{-0.04}$	1.64/3	–	–	–	–	–
Cumulative	1.29 ± 0.06	0.20	25.05/50	$0.91^{+0.13}_{-0.14}$	$2.14^{+0.29}_{-0.24}$	0.28	$2.37^{+0.36}_{-0.23}$	3.38/48

Notes. The best-fitting results from SHERPA. The definitions of the models and their parameters are given in equations (2) and (3), and the text. The broken power-law model was fitted to the cumulative XLF only. [a]Value of minimized statistic/degrees of freedom; we use the χ^2 statistic (CHI2GEHRELS) to fit the differential XLF, and the cash statistic (CSTAT: Cash 1979) to fit the cumulative XLF. All best-fitting parameter values are reported with 1σ errors.

extensive population studies of the last decade (Grimm et al. 2003; Swartz et al. 2011; Mineo et al. 2012a) reported on features at a similar luminosity. Even if the break is present, another possibility is that a feature resembling a break may be artificially caused by the considerable ($\sigma/\langle N(>L)\rangle \sim 1.7$) dispersion in the normalization of the individual XLFs, which is comparable with that observed by Mineo et al. (2012a) at the same luminosity threshold ($\sigma/\langle N(>L)\rangle \sim 1.5$, see discussion in section 7.1 of Mineo et al. 2012a). A second means of artificially inducing a break could be by overestimating the completeness of the sample, i.e. incompleteness could act to turn down the XLF slope at lower luminosities if we have not accounted for it properly (see the discussion in section 3 of Fabbiano 2006). However, this is eminently testable in our data as several of our galaxies are complete well below the putative break (cf. Table 3); hence, the number of sources above and below the break in these galaxies can be compared to the numbers in the galaxies with sensitivity limits closer to the break luminosity. We find that 6/11 ULXs are below the putative break in the five nearest host galaxies (NGC 1068, NGC 1365, NGC 7552, NGC 4418 and NGC 4194); this compares to 21/42 in the more distant LIRGs. Given the small numbers of objects involved these numbers appear consistent, hence there is no reason to suspect that incompleteness is inducing the putative break feature. If the break is a real feature intrinsic to the ULX population, it immediately becomes very interesting as the steepening of the XLF slope above L_b may suggest that much of the deficit in ULXs is originating above this putative break. We will further discuss the possible physical explanation of the very putative break in Section 4.2.

As a check, we also used SHERPA to fit the differential XLF. In this case we had to assume χ^2 statistics (CHI2GEHRELS) and fit the binned differential XLF. This is, strictly speaking, not appropriate for the number of sources per luminosity bin. The reduced fitting statistic is substantially below unity, primarily as a consequence of the small number of bins. However, we note that the best-fitting parameters for the two forms of the XLF obtained with the procedure described above for a pure power-law model (Table 9), are in full agreement with those provided by the ML fitting (Table 8).

4 DISCUSSION

4.1 X-ray spectral results

In Section 3.1.1, we presented an analysis of the stacked spectra for three groups of ULXs, segregated by their observed luminosity. The analysis of stacked spectra is notoriously difficult to interpret, as summing spectra that may have a variety of underlying levels of absorption and intrinsic forms may not necessarily reveal anything about the population of sources contributing to the stack. However, in the case of the stacked spectra we create, we see one remarkable result; the stacked spectrum of the sources below $\sim 2 \times 10^{39}$ erg s^{-1} appears markedly different to the stacked spectra of the two more luminous groups. Both the power-law continuum fit and MCD model fit show that the lowest luminosity spectrum is significantly softer than that in the two more luminous groups, which are statistically indistinguishable from each other.

Further interpretation is difficult due to the uncertainty in the absorption column, which may vary substantially for the individual ULXs given that LIRGs are known to contain substantial quantities of cold, neutral gas (Mirabel & Sanders 1988). This would work to distort any underlying spectrum – for example, if the average spectrum was heavily absorbed, just a handful of non-representative, low-absorption sources would 'fill-in' the soft end of the spectrum and lead to a relatively low column being measured. Indeed, this may be part of the reason for the columns on the MCD fits being consistent with zero, although they are substantially higher than the enforced Galactic foreground upper limit for the sample of $<5 \times 10^{20}$ cm^{-2} in the power-law fit. We therefore do not directly interpret the power-law slopes or disc temperatures in light of Galactic binaries and/or other ULXs. We do note, however, that previous analyses have suggested transitions in ULX spectra at similar luminosities. Both Gladstone & Roberts (2009) and Yoshida et al. (2010) examine ULXs in the interacting galaxies NGC 4485/90 (and also M51 in the latter paper), and note a change from power-law-like spectra dominating, to more disc-like spectra at $\sim$2–3 $\times 10^{39}$ erg s^{-1}, that they also reconcile with the objects becoming substantially super-Eddington beyond that luminosity. Furthermore, the detailed ULX spectroscopy of Gladstone et al. (2009) and follow-up work by Sutton et al. (2013b) show that below $\sim 3 \times 10^{39}$ erg s^{-1} most ULXs have disc-like spectra in the wider *XMM–Newton* bandpass; above this luminosity their spectra resolve into two components, with roughly equal numbers dominated by either the hard or soft component. This is again interpreted as a transition from an $\sim$ Eddington rate phase, to a super-Eddington state. Based on their work, we can speculate why our stacked spectra may harden at higher luminosities – if there is substantial absorption present in the LIRGs, it will act to extinguish the signal from the soft ULXs more efficiently than the harder objects. A salient example of this effect is the extreme ULX in NGC 5907, where a high foreground column may hide a large soft contribution to its spectrum (Sutton et al. 2013a). This would therefore preferentially hide the softer ULXs at high luminosities, leaving only the hard spectrum objects to contribute to the stacked spectrum.

One object in our sample had sufficient counts in its *Chandra* X-ray spectrum for us to analyse it separately. We found the spectrum of CXOU J024238.9-000055 to be very hard, with a power-law of photon index $\Gamma = 0.75 \pm 0.1$ providing an acceptable fit to the data. This result is consistent with previous studies, which also found that the photon index is very hard (Smith & Wilson 2003; Swartz et al. 2004; Berghea et al. 2008). Smith & Wilson (2003) interpret the hard spectrum of this ULX as inverse Compton scattering of

synchrotron emission in a jet. However, they also noted the presence of a broad feature that dips below the continuum level at ∼1.7 keV, and suggest that this may be a spurious feature resulting from an artefact in the gain table of the *Chandra* ACIS-S instrument. We have re-analysed the data with the latest *Chandra* calibration data base that includes corrections for such features,[21] but still find the feature to be present. We therefore characterized it using a single Gaussian absorption line; this produced a good fit to the data, but produced a broad (∼80 eV width) line centred at 1.68 keV, that we struggle to attribute to any single physical absorption feature.

We therefore considered an alternative solution – that the feature is the result of absorption in a range of partially covering, partly ionized material (a 'warm' absorber model). Interestingly, a similar model was suggested as a way of producing the apparent two-component *XMM–Newton* spectra of ULXs by Gonçalves & Soria (2006), and was also used to describe the spectrum of a ULX in NGC 1365 by Soria et al. (2007). In the latter paper, they propose that the ionizing material may be in an outflow, with its origins in the formation and subsequent ejection of a Comptonizing region above the inner accretion disc. Interestingly, the best-fitting parameters from Soria et al. (2007) – $N_{\rm H}$, Γ, ξ – broadly agree with our best-fitting parameters. Our value of ionization parameter $\xi \approx 158 \pm 87$ for CXOU J024238.9-000055 corresponds to the ionized material being located at a distance $R < L/(\xi N_{\rm H})$, which for the ionizing luminosity (i.e. intrinsic $L_{\rm X}$ extrapolated from the model fit between 13.6 eV and 20 keV) gives a maximum radius for the material of 3.5×10^{15} cm ($=1.2 \times 10^{9} R_{\rm g}$ where the gravitational radius $R_{\rm g} = 2GM_{\rm BH}/c^2 = 30$ km for a $10\,{\rm M}_{\odot}$ BH). Clearly, this is located in the proximity of the ULX, but not close to the inner regions of the disc, consistent with material that has been ejected from the system in some sort of outflow. We note that a massive, likely highly ionized outflow is a prediction of super-Eddington models (e.g. Poutanen et al. 2007); evidence has recently been sought for it by looking for partially ionized Fe K lines in spectrally hard ULXs (e.g. Walton et al. 2012, 2013), with little success. However, signatures of partial ionization may be preferentially located in the softer part of the X-ray spectrum (Middleton et al. 2014a), that is easier to see in objects that are wind-dominated – here, we may be seeing precisely that.

4.2 Why is there a deficit of ULXs in LIRGs?

In this paper, we have presented evidence for a significant deficit in the number of ULXs detected in this sample of LIRGs, compared to the expectation based on the relationship between the number of ULXs and the SFR in nearby galaxies. This manifests itself both in the raw numbers – we expect to detect ∼500 ULXs in this sample if it follows the number of ULXs per unit SFR relation of Swartz et al. (2011), compared to just 53 detections – and in the characteristics of the XLFs we construct from our detections. In the latter, the normalization of the differential XLF is a factor of ∼5 lower at $10^{39}\,{\rm erg\,s^{-1}}$ than the most complete previous analysis of the HMXB XLF (Mineo et al. 2012a), and although the differential slope is consistent within errors with previous work the cumulative form has a slope that is steeper than that found for most star-forming systems (cf. Fabbiano 2006 and references therein), implying fewer sources are present at high luminosities. This steep slope may be the result of a break in the XLF at $\sim 2 \times 10^{39}\,{\rm erg\,s^{-1}}$; at energies below the break we see a slope similar to that in star-forming galaxies ($\gamma_1 \approx 0.9$). If this shallow slope were extrapolated to luminosities above $10^{40}\,{\rm erg\,s^{-1}}$, we would expect to see ∼7 ULXs in that regime; instead we see none. In this section, the possible explanations for the deficit will be discussed.

4.2.1 *A real deficit or observational effects?*

A pertinent question we must therefore ask about the presence of this deficit is simply: why? A first consideration is whether we really detect all the ULXs that are bright in the 0.3–10 keV regime in the host galaxies. In this regard, we are certainly using the best instrument available for this study; the exquisite sub-arcsecond spatial resolution of *Chandra* is unparalleled in this respect, allowing us by far the clearest X-ray view of these regions, and minimizing any source confusion. We cannot completely avoid this – for example, the nucleus of M82 hosts at least two extreme ULXs (e.g. Feng & Kaaret 2007), that we would not resolve if placed at the distance of our furthest LIRGs. However, we will miss very few ULXs ($\lesssim$10 per cent) due to sensitivity issues in these galaxies (see Section 2.2.3), with the sample essentially complete in terms of sensitivity to ULX detection.

But while we may have sufficient sensitivity to detect ULXs over the projected area of the galaxies, this could be compromised locally by extended diffuse X-ray emission. In particular, the extended source detections that we reject from our point source detection analysis might physically comprise a mixture of extended and faint point-like X-ray emitters, and so could hide ULXs that otherwise would have been detected. To determine whether this has a large influence on our sample, we consider that the diffuse emission is likely to be spectrally soft in SF-dominated galaxies, and so dominant only below 2 keV (cf. Pietsch et al. 2001; Franceschini et al. 2003; Jenkins et al. 2004; Mineo, Gilfanov & Sunyaev 2012b); hence, the hidden ULXs would be visible as point-like sources at higher energies (above 2 keV). However, we face the problem that we do not have high photon statistics in this regime, and our sensitivity is relatively poor. In fact, the best way to proceed is to revisit our initial source lists for each galaxy where we already have a complete record of the detectable objects above 2 keV as our hard band detections. We therefore determined which of the hard band detections did not make it into our final source catalogue, and investigated why.

In total, there are 17 objects that have full band luminosities in excess of the ULX threshold of $10^{39}\,{\rm erg\,s^{-1}}$, which are detected as hard band sources but do not make the final source list. For each of these objects, we revisited their hard band data and ran the SRCEXTENT algorithm to determine whether they appeared point-like or extended, although we caution that in several cases the photon statistics were limited and so the results may not be conclusive. We found that a total of four sources were spatially extended above 2 keV; the remaining 13 were consistent with point-like objects. However, nine of these point-like objects were located with 5 arcsec of the nuclear position of their host galaxy and so are rejected from consideration. Of the four remaining objects, two that lie in Arp 299 are questionable ULX detections as they are coincident with plausible contaminants in the host galaxy (a supernova remnant, and the secondary nucleus in this merging system). Hence, only two plausible ULX candidates remain, one each in NGC 1068 and Arp 299. Both objects were originally rejected as extended full band sources, but are resolved to be point-like sources in the hard band.

[21] In a correspondence with the *Chandra* X-ray centre help desk, we were informed that this issue was corrected for in calibration data base (CALDB) versions 3.0.0 and later.

Given that we can only do this for two objects, this indicates that we are not missing a significant population of ULXs by rejecting extended sources.

Although the nuclei of the galaxies cover a relatively small region of their surface area, we may miss a proportion of the ULX population by excluding this region – see Lehmer et al. (2013) for an example that would be excluded from the nearby starburst galaxy NGC 253. This is particularly pertinent as the SF in LIRGs can be very centrally peaked, so by excluding the nucleus we may be rejecting a region containing a large fraction of the galaxy's SF, and so a proportional number of ULXs. There will, however, be observational difficulties with detecting such a population – as Fig. 1 shows, the central regions tend to have far higher surface brightness in X-rays and possible spatial complexity compared to the outer regions. But, given the high spatial resolution of the *Chandra* telescope mirrors (0.5 arcsec on-axis resolution), we should have the imaging power to resolve the nuclear region of each galaxy, and detect the brightest point-like sources if they are abundant in that region. Yet, we only find three examples of galaxies with more than a single source detection in the nuclear region, and in one of these objects (in NGC 1365) the source furthest from the nuclear position is relatively faint ($\sim 10^{38}$ erg s^{-1}). Conversely, 15 out of 17 galaxies have at least one source detection (in two cases – NGC 4418 and NGC 5653 – there are two detections) in the nuclear region with a luminosity in the ULX regime, although seven of these are spatially extended sources in the full band (of which five are resolved to point sources above 2 keV). Eight of these are galaxies with a suspected/confirmed AGN;[22] and although we detect a source in each galaxy that we regard as lacking an AGN based on previous evidence, we cannot reject an AGN nature for any of these objects without further observations and detailed analyses that are beyond the scope of this paper. Thus, the situation is unclear on how many of these detections could be bona fide ULXs in the nuclear region. However, the total number of detected ULXs in the nuclear regions appears significantly smaller (<17, likely half that amount given the evidence for AGN) than the numbers of ULXs detected outside the nuclei. So the deficit of ULXs seems to appear significantly worse in the central regions of the galaxies, albeit with some caveats about the difficulty of observing in that region.

To investigate this further, we examined the total flux within each 5 arcsec radius nuclear region, excluding the flux from the detected point sources, in order to place an upper limit on the possible residual flux from ULXs hidden within the diffuse emission. This analysis was only performed for the seven galaxies in which we have no multiwavelength evidence for the presence of an AGN, to avoid any complex spatially extended emission that could be related to such an object. For three galaxies – NGC 7552, NGC 838 and NGC 23 – there are a sufficient number of counts ($\gtrsim 300$) to extract a spectrum of the emission within the 5 arcsec nuclear region. The spectra were fitted with a two component model comprising an optically thin thermal plasma (MEKAL in XSPEC) plus a power-law continuum, both subject to the same absorption column. The first component can be used to represent the diffuse emission from the active star-forming region, whilst the latter represents the integrated emission from XRB systems in the region. Both NGC 7552 and NGC 23 displayed similar residual nuclear spectra, with moderate absorption ($5–20 \times 10^{20}$ cm^{-2}) and similar plasma temperatures and power-law photon indexes ($kT \sim 0.6–0.7$ keV; $\Gamma \sim 2$), whereas NGC 838 appeared somewhat more absorbed, with a cooler diffuse component ($N_{\rm H} \sim 7 \times 10^{21}$ cm^{-2}; $kT \sim 0.15$ keV; $\Gamma \sim 2.5$). We estimated the observed flux from XRBs in each galaxy nucleus from the power-law component in each object. In order to do the same for the galaxies with too few counts for spectral analysis, we extracted the total residual count rates in the nuclear region of each galaxy, and then applied a factor of 0.5 multiplier to each total to account for only ∼50 per cent of counts originating in the XRB population of each galaxy (which was estimated from the fitted spectra). We then converted these counts to fluxes using a typical ULX-like spectrum, consistent with the power-law continua seen in the three bright galactic nuclei ($N_{\rm H} \sim 1.5 \times 10^{21}$ cm^{-2}, $\Gamma \sim 2$). The estimated observed luminosities in the power-law component for each galaxy are shown in Table 10.

Table 10. Upper limits on the number of ULXs hidden within the diffuse component of each galaxy nucleus without evidence for an AGN.

Galaxy	$L^a_{\rm PL}$ (10^{39} erg s^{-1})	$N^b_{\rm ULX,hid}$	$(f_{\rm nuc}/f_{\rm gal})^c_{\rm IR}$
NGC 7552	18	3.8	0.2
IC 5179	7.1	1.5	0.17
NGC 838	30	6.5	0.49
NGC 5653	7.9	1.7	0.2
NGC 3221	2.2	<1	0.08
CGCG 049-057	1.3	<1	0.81
NGC 23	33	7.2	0.45

Notes. [a]Total observed luminosity estimate for the hard power-law component in each galaxy nucleus. [b]Estimated upper limit on the number of ULXs hidden within the diffuse emission in this region (see text for details). [c]Fraction of the total 8 μm flux from each galaxy residing in the nucleus.

Assuming that the luminosity distribution of XRB systems in the nuclear region of the LIRGs follows the Mineo et al. (2012a) XLF, we converted the power-law luminosity into a number of ULXs using that XLF. In each case, we worked out the normalization required to give the integrated luminosity by integrating under the XLF in the 10^{37}–10^{40} erg s^{-1} range, and then using this to calculate the number of ULXs present, that we show in Table 10. A strict upper limit would simply assume that each ULX has a luminosity of 10^{39} erg s^{-1}; however, a population of ULXs should have a range of luminosities, and integrating under the XLF accounts for this. What this method does not account for is that the brightest objects should still be detected as point sources, even within bright diffuse emission, by *Chandra*; but as we saw above the number of such objects detected within the nuclear regions is small. Given that these nuclei are likely to be far more complex than our simple modelling allows for, and may contain additional components that contaminate the hard band (e.g. hard diffuse emission, extended reflection nebulae from an unseen AGN), we consider our $N_{\rm ULX,\,hid}$ estimate as a reasonable upper limit on the number of ULXs that may be hidden within these nuclei. In total we may have up to ∼21 ULXs hidden within these galaxies, or ∼3 per nucleus. Over the whole sample this would extrapolate to ∼50 ULXs, or a rough doubling of our ULX numbers, and hence an increase in ULX incidence to 0.4 ULX per unit SFR.

As an independent check of the effect of excluding the nuclear region, we estimated the fraction of the global SF we are excluding for each galaxy. We used the FIR emission as mapped by 8 μm

[22] Interestingly, the two galaxies without a point source detection in their nucleus – ESO 420-G013 and IC 860 – have some evidence for the presence of an AGN; looking at Fig. 1 they do have X-ray emission in their nucleus that presumably was too extended for the WAVDETECT algorithm.

Spitzer images[23] as a proxy for the SFR, and in each case, we corrected for the contribution of an old stellar population to the 8 μm flux using the 3.6 μm images and equation 1 of Calzetti et al. (2007). Then, we took the ratio between the SFR in the central 5 arcsec nuclear region and that of the rest of the galaxy (out to the R_{20} ellipse), again for the seven galaxies with no evidence for an AGN. We found that the nuclear region contribution to the total SFR, $(f_{\rm nuc}/f_{\rm gal})_{\rm IR}$, varied widely, between ∼8 and ∼ 80 per cent in the AGN-less galaxies (see Table 10). However, there was only one case in which it exceeded 50 per cent, so if we take this as the upper limit on the coarse average contribution from the nuclear region and apply that as a correction to the regions outside the nucleus across the whole sample, then we can set an upper limit on our global incidence of ULXs in the LIRG sample of 0.4 ULXs per unit SFR. Interestingly this upper limit coincidences with the result from the flux analysis demonstrated above.

However, despite the suggested rise in ULX numbers from the upper limits place on the nuclear regions, if we combine the observational effects described above, it is very implausible that they will result in a factor of 10 increase in ULX detections. We therefore regard the deficit as a real effect, and consider physical origins for it.

4.2.2 *Possible explanations for the deficit*

So, what is the physical origin of the deficit of ULXs in the LIRGs? First, we would not expect that all ULXs come from young stellar populations. There are ULXs seen in elliptical galaxies that must be related to their LMXB populations, and we should expect all galaxies with old stellar populations to possess a similar underlying population of LMXBs that scales with the mass of the system (Colbert et al. 2004; Lehmer et al. 2010). This is not accounted for by Swartz et al. (2011); their number of ULXs per SFR that we base our deficit deduction on will contain ULXs from both populations. However, this cannot lead to the deficit of ULXs in the LIRGs, for the simple reason that our LIRG sample contains ∼four times more mass than the combined mass of the nearby galaxies in Swartz et al. (2011), at $\sim 1.3 \times 10^{13}\,{\rm M}_\odot$ versus $\sim 3.5 \times 10^{12}\,{\rm M}_\odot$;[24] thus, we would expect our sample to possess more LMXB ULXs, that would act to increase the number of ULXs per SFR. In fact, using the estimate of Feng & Soria (2011) and making a conservative (factor 2) correction for the high background contamination in the elliptical sample of Walton et al. (2011), we might expect 0.5 LMXB ULXs per $10^{11}\,{\rm M}_\odot$ of galaxy mass. We would then expect that less than one fifth of the Swartz et al. (2011) ULXs (∼17) are LMXBs; however, we would expect more LMXB ULXs in our sample (∼65) than we observe ULXs in total. Given the high SFR that accompanies the high mass of our sample systems, this serves to emphasize that a real deficit in ULXs is present in the LIRG sample.

Could this deficit be due to some factor inhibiting the formation of ULXs in the environment of the LIRGs? An obvious property that might suppress the formation of ULXs, given recent studies (e.g. Mapelli et al. 2011; Basu-Zych et al. 2013a,b; Prestwich et al. 2013; Brorby, Kaaret & Prestwich 2014), could be the relatively high metallicity of the LIRGs. A good comparator sample for the LIRGs in this respect is the high-metallicity galaxies sample of Prestwich et al. (2013), that was demonstrated to show a much lower incidence of ULXs per unit SFR than a sample of extremely metal poor galaxies. A comparison of our Table 1 and table 9 of that paper shows that (where available) both samples have a very similar spread of metallicity; and indeed table 10 of Prestwich et al. (2013) quotes an $N_{\rm ULX}$ per SFR of 0.17 ± 0.042 per ${\rm M}_\odot\,{\rm yr}^{-1}$, identical within errors to our value of 0.2 ± 0.05 per ${\rm M}_\odot\,{\rm yr}^{-1}$. However, Prestwich et al. (2013) used a different method to calculate SFR (Calzetti et al. 2010, based on the Hα and 24 μm fluxes); when we use our SFR calculation method on their sample of galaxies we find that the SFR drops by a factor ∼6 to a total of $16.77\,{\rm M}_\odot\,{\rm yr}^{-1}$ across the whole sample.[25] Hence, the number of ULXs per SFR for this sample increases dramatically, up to 1.04 ± 0.26 per ${\rm M}_\odot\,{\rm yr}^{-1}$; notably this is lower than the average relation in nearby galaxies, but it is again significantly higher than the number of ULXs per SFR in the LIRGs (and is also significantly higher than the upper limits accounting for the excluded nuclear regions derived in the previous section). Hence, given the similar metallicities of the two samples,[26] we conclude that the relatively high metallicity of the LIRGs appears insufficient reason on its own to explain their deficit in ULXs.

One reason for suspecting that metallicity affects the incidence of ULXs is the possibility that larger BHs (the MsBH class, with masses between 20 and 100 ${\rm M}_\odot$) might form in low-metallicity regions. Conversely, very few such objects should be seen in higher metallicity regions. If such objects, accreting at ∼ Eddington, constitute a large proportion of ULXs up to the HMXB XLF break, then an interesting consequence should be that the XLF break shifts to lower luminosities in high-metallicity environments. This is precisely what is suggested by the very putative break in the cumulative XLF, with the break apparently shifting down by a decade in luminosity to the Eddington limit for an ∼16 ${\rm M}_\odot$ BH, compared to the break found in the Mineo et al. (2012a) XLF. The lack of ULXs with luminosities above $10^{40}\,{\rm erg\,s}^{-1}$ certainly appears consistent with this scenario. In addition, this result is supported by the spectral changes seen in this sample, with the change in spectral form either side of the same luminosity as the putative XLF break suggesting the transition between stellar-mass BHs accreting at ∼ Eddington, and those at super-Eddington rates. However, this is not supported by wider spectral studies that see a similar pattern in ULXs located in all galaxy types (Gladstone et al. 2009: Sutton et al. 2013b) – if a large proportion of ULXs were ∼ Eddington accretion on to MsBHs, we would see the disc-like spectra reported by Gladstone et al. (2009) extend up to the XLF break in many sources, but they instead are mainly seen below $3 \times 10^{39}\,{\rm erg\,s}^{-1}$, seemingly ruling this out. One interesting scenario remains, though – the factor of 10 drop in the XLF break luminosity could still be due to a drop in the mass of the compact objects, if the objects below the break are predominantly super-Eddington neutron stars (NSs), that reach maximal super-Eddington luminosities at the putative XLF break. This might be the case if the high metallicities impede the formation of all BHs, not just MsBHs, and the change in spectrum might then be the difference between the super-Eddington NSs and an underlying population of BHs. Clearly, this is highly speculative,

[23] http://sha.ipac.caltech.edu/applications/Spitzer/SHA/

[24] The total mass of the LIRGs was taken from table 1 of Lehmer et al. (2010).

[25] There was no *IRAS* data available for NGC 4625 in the high-metallicity sample; we retained the estimate used by Prestwich et al. (2013), but note that this will not adversely affect the results as it had the smallest estimate of SFR in the sample at $0.22\,{\rm M}_\odot\,{\rm yr}^{-1}$.

[26] We caution that one caveat here is that further, systematic measurements of metallicity, that supersede the current disparate methods, are required to confirm that the samples do overlap in metallicity.

and requires a great deal of improvement in data quality in order to investigate this hypothesis. First, we need to confirm the presence of the break; then we need to identify the source populations either side of it. This will almost certainly require next generation X-ray observatories that can begin to disentangle BHs and NSs at large distances based on their observational characteristics.

The next possibility we consider that might cause the deficit of ULXs is whether the stellar populations of the LIRGs are too young to allow a population of ULXs to form. As ULXs are composed of a compact object accreting material from a stellar companion, they will require time to evolve from an initial massive stellar binary system. This inevitably introduces a lag between the start of SF in a system, and the appearance of ULXs. According to Linden et al. (2010), the number of ULXs formed in solar metallicity environments peaks at ∼4–5 Myr after the beginning of SF, and a lag of up to ∼10 Myr is required to see the peak for ULX populations formed in a sub-solar metallicity medium. These ages are consistent with the resolved stellar population ages around two nearby ULXs, that are of the order of $\lesssim$ 20 Myr (Grisé et al. 2008; Grisé et al. 2011). So the critical question is: how long is it since the SF began in the LIRGs? Older studies, based on the correlation between the Brackett-γ and FIR emission, estimates SF ages in LIRGs at between 10 and 1000 Myr (Goldader et al. 1997). However, later work based on the spectral energy distributions of LIRGs and ULIRGs (ultraluminous infrared galaxies) from near-IR to radio wavelengths suggests SF time-scale of ∼5–100 Myr (Vega et al. 2008; see also Clemens et al. 2010). In fact, the SF ages of a few individual LIRGs have been reported in previous works: for example, 57 Myr for Arp 299 (Vega et al. 2008; Clemens et al. 2010), and 30 Myr for both NGC 7552 and NGC 4194 (Takagi, Arimoto & Vansevičius 1999). Thus, it seems unlikely that the LIRGs are too young for their populations of ULXs to switch on.

However, the age calculations above assume a single age for the newly formed stellar population. This might not be a good assumption because the SF activity is unlikely to be uniform throughout the galaxies (see e.g. Mineo et al. 2013); it is possible that SF may have begun more recently in some regions in the galaxies than in other areas. For example, the spatial study of NGC 5135 by Bedregal et al. (2009) suggests that the most recent star-forming areas in the galaxy could be ∼0.5–1 Myr younger than other regions. Moreover, they also suggest that NGC 5135 might host two recently formed stellar populations with different ages: a new population that formed ∼6–8 Myr ago, and a second, older stellar population of $\gtrsim$200 Myr age. Thus, simply assuming the same stellar age along the whole galaxy might not reflect the real history of SF in LIRGs. However, even bearing these caveats in mind, we would realistically require the vast majority of the SF in the LIRGs to have started within the last 5 Myr for the populations of ULXs to be significantly suppressed; given the ages quoted above this is very unlikely. Therefore, while this effect may have some influence in the LIRG sample, we regard it as unlikely to be the major factor in the ULX deficit.

So, if the deficit of ULXs in LIRGs is unlikely to be caused by metallicity effects or a very young stellar population, then is there another possibility that may act to reduce the number of detected ULXs? The answer is potentially revealed in the global $N_{\rm ULX}$–luminosity relations discussed in Section 3.2.1. In particular, Smith et al. (2012) find similar ratios in a sample of interacting galaxies taken from the Arp catalogue – they find an enhancement in the $N_{\rm ULX}/L_B$ compared to normal galaxy samples, but in their most IR luminous objects they find the $N_{\rm ULX}/L_{\rm FIR}$ ratio significantly suppressed. They suggest two reasons for this: either the FIR luminosity is significantly enhanced by nuclear activity; or the large columns of gas and dust in these objects are obscuring a large fraction of the ULX population. In our work, we have explicitly removed possible AGN contamination from the FIR fluxes using the method of Mullaney et al. (2011), and then shown that these ratios are the same for LIRGs that both host and do not host AGN; hence, we rule out the first scenario. We therefore favour the second explanation – that the suppressed $N_{\rm ULX}/L_{\rm FIR}$ ratio in LIRGs could be a result of missing many ULXs due to their signal being extinguished by the high absorption columns in these galaxies due to dust attenuation. Indeed, Lehmer et al. (2010) suggested that an apparent lack of luminosity in X-rays present in the LIRGs, compared to expectation, might be due to dust obscuration. Furthermore, such an effect is seen also in normal star-forming galaxies (fig. 11 of Mineo et al. 2012a) as well as in the sample of Local Lyman Break Galaxy Analogues which is shown in the left-hand panel of fig. 7 of Basu-Zych et al. (2013b). Indeed, that is also consistent with the other relationships we see – both X-rays and blue light relate to young stellar populations, so explaining the proportionality relationship between the two; but the unusually high number of ULXs per blue luminosity in these galaxies is plausibly due to a faster loss of blue light than X-rays in the absorbing material.

Hence, we have a plausible explanation for the overall deficit of ULXs per SFR in the LIRG sample; we do not see most of them because they are hidden behind the material fuelling the high SFR in these objects. But is this consistent with the columns of material we expect in LIRGs? We can quantify the column densities required to support this scenario by examining how the detectability of sources with *Chandra* depends on their intrinsic spectrum, their observed luminosity, their distance and the intervening columns. If we assume 20 ks exposures (typical for our sample), and a power-law form for our spectra, then we can use WEBPIMMS to calculate the dependence of the detected counts on absorption column and distance to the ULXs, which we show in Fig. 6. Taking a minimum detectability threshold of six counts (cf. Table A1) demonstrates that the effective extinction of the ULXs strongly depends on distance to the host galaxies. In the nearest system (NGC 1068, at 14 Mpc) a faint ULX (at 10^{39} erg s^{-1}) would be fully extinguished by a column of $\sim10^{23}$ cm^{-2}, whilst a brighter object (with luminosity 10^{40} erg s^{-1}) requires a higher column of $\sim10^{24}$ cm^{-2} to be obscured from our view. These columns reduce with distance – at 30 Mpc the equivalent columns are $\sim10^{22}$ and a few times 10^{23} cm^{-2}, respectively, while at 60 Mpc even minimal column ($\sim10^{20}$ cm^{-2}) will cause a faint ULX to be missed, and $\lesssim 10^{23}$ cm^{-2} is required to obscure a bright ULX. Crucially, these columns are consistent with those seen in LIRGs. For example, Genzel et al. (1998) reported that some ULIRGs have high optical extinctions, $A_{\rm V} \sim 1000$, corresponding to a column density of $\sim 2 \times 10^{24}$ cm^{-2} (using the conversion of Güver & Özel 2009 where $N_{\rm H} = 2.21 \times 20^{21}$ cm^{-2} $A_{\rm V}$). Indeed, a FIR spectral study of NGC 4418 by *Herschel*/PACS revealed a very high value of column density in the nuclear region of the galaxy, $N_{\rm H} \sim 10^{25}$ cm^{-2} (González-Alfonso et al. 2012). Clearly, these high columns are commensurate with completely obscuring ULXs from our view.

One caveat of this conclusion is that it appears unlikely that there is a steady gradation of column as one enters the LIRGs. In such a situation one might expect to see a range of obscuring columns building up to the high central values, and this would lead to a population of absorbed, and so spectrally hard, but not completely obscured ULXs. We see no such population in the LIRGs, with just one ULX being a hard band only detection, arguing that the absorbing material is a relatively dense medium enshrouding the ULX population. We speculate that such a medium might produce the very putative break in the XLF, but only if the brighter ULXs are

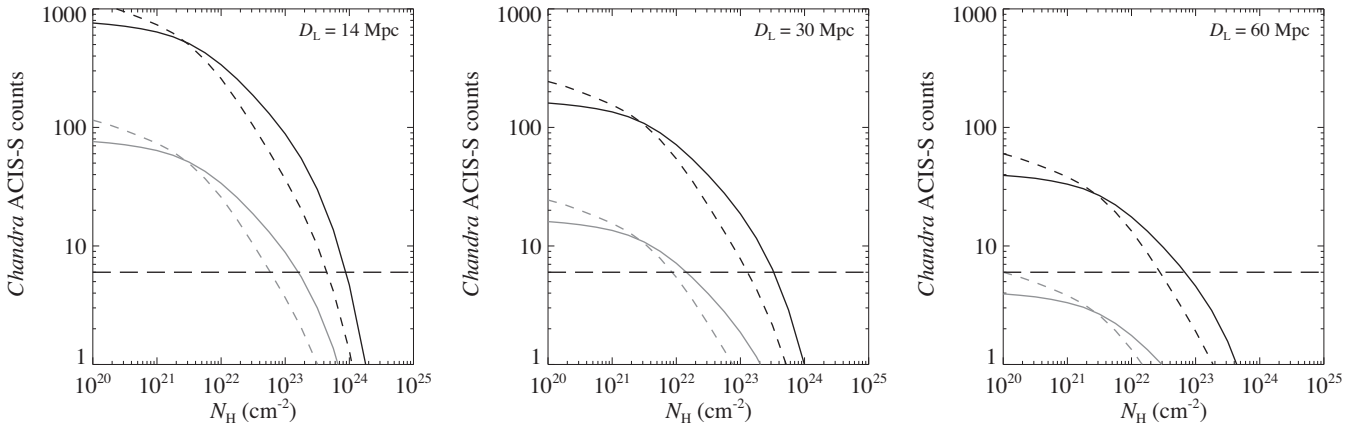

Figure 6. Simulated *Chandra* ACIS-S counts detected from ULXs as a function of column density (N_H), calculated at luminosity distances of 14 (left), 30 (middle) and 60 (right) Mpc. Assuming 20 ks observations, WEBPIMMS was used to simulate the number of counts detected from ULXs with photon indexes of 1.5 (solid line) and 2.5 (dashed line). Both calculated values for faint (10^{39} erg s^{-1}; grey lines) and bright (10^{40} erg s^{-1}; black) ULXs are plotted here. The horizontal dashed line indicates the detection limit – the minimum number of counts where ULXs are detected as point sources in our observational data by the WAVDETECT algorithm.

preferentially buried behind the screen of material.[27] Interestingly, this is also entirely consistent with the acute lack of ULX detections in the nuclear regions discussed in the previous section; we would expect the innermost regions of each LIRG to be the most deeply enshrouded in dust and gas, and so the most difficult to observe ULXs in.

Finally, interesting supporting evidence for the obscuration scenario is provided by another exotic phenomenon that appears to be underrepresented in LIRGs – core-collapse supernovae (CCSNe). Optical surveys for these explosive transients reveal that up to 83 per cent of the expected CCSNe (given the calculated SFR) are missing (e.g. Horiuchi et al. 2011; Mattila et al. 2012). Again, this is directly attributable to the very dusty environments of the LIRGs, which obscure and so extinguish the emission from these objects.

5 CONCLUSION

In this paper, we have studied the population of ULXs present in a sample of 17 nearby, low foreground absorption LIRGs, based on *Chandra* observations. We detect a total of 53^{+16}_{-13} ULXs in the galaxies, among a total of 139 point X-ray sources, of which we expect less than one fifth to be background objects. We consider the sample to be essentially complete in ULX detection. Our main results can be summarized as follows.

(i) The source spectra were stacked into three groups as a function of source luminosity. The stacked spectrum of the lowest luminosity sources ($L_X < 2 \times 10^{39}$ erg s^{-1}) is significantly softer than the two more luminous stacks, that are indistinguishable from one another. This is consistent with a change in accretion state for 10 $M_\odot$ BHs as they progress from $\sim$ Eddington rate accretion into a super-Eddington, ultraluminous state.

(ii) In one object (CXOU J024238.9-000055 in NGC 1068), we have sufficient statistics to study its spectrum individually. Although its spectrum can be acceptably fitted with a power-law continuum, this leaves a large residual at $\sim$1.7 keV. We find that this can be modelled by the presence of a partially ionized partial covering medium, located within $10^9 R_g$ of the ULX, which might be material expelled from the system in a radiatively driven outflow, as expected for super-Eddington accretion.

(iii) The LIRGs possess significantly fewer ULXs per unit SFR than nearby 'normal' galaxies, by a factor of $\sim$10. This deficit also manifests itself as a lower normalization of the differential XLF than for nearby HMXB samples, and a steeper slope to the cumulative XLF than nearby star-forming galaxies. This is very unlikely to be the result of more LMXB ULXs in the normal galaxy sample; nor is it likely to be due to observational effects such as source confusion, or ULXs missed by the detection code due to being embedded in diffuse emission. Very few of the missing ULXs are detected in the nuclear regions we initially exclude from our analysis; however, correcting for those ULXs that may be present based on sources hidden within a diffuse nuclear component, or the SFR of the nuclear region, still presents upper limits significantly below the number of ULXs expected from normal galaxies.

(iv) Metallicity may have some influence on ULX numbers. It might suppress the formation of massive stellar remnants, which may be consistent with a very putative break found in the cumulative XLF and the total absence of ULXs above 10^{40} erg s^{-1}. However, we regard this effect as unlikely to explain the whole deficit.

(v) A second factor that may have some impact on the deficit is the lag between SF starting and the appearance of ULXs. However, given the stellar ages of newly formed populations in LIRGs are typically estimated to be older than 5 Myr, this provides sufficient time to turn ULX populations on, so we are disinclined to regard this as a major contributor to the deficit.

(vi) The relatively high ratio of N_{ULX}/L_B, and very low ratio in N_{ULX}/L_{FIR}, of the LIRGs compared to normal galaxy samples point to a very plausible explanation for the main cause of the deficit – a large part of the ULX population is hidden behind the high columns of gas and dust present in these systems. We show that the columns of absorbing material present within LIRGs are sufficient to fully obscure a population of ULXs. This is supported by the the detection of far fewer ULXs per unit SFR in the nuclear regions of the LIRGs where we expect the obscuration to be greatest, and by a similar observational deficit in CCSNe, that should also be more numerous in LIRGs than is observed.

[27] There is perhaps a hint of the more luminous ULXs being more absorbed in the harder stacked spectra of these objects, although the measured absorption columns do not significantly vary between the three luminosity bins.

If there are large hidden populations of ULXs in the most massive star-forming galaxies in the Universe, as is suggested by this sample of LIRGs, then this has interesting implications. First, given the flat XLFs of star-forming systems, it can be shown that ULXs dominate their hard X-ray luminosity. However, if these objects are hidden from view, then the observed hard X-ray luminosity of these systems will be largely suppressed below its intrinsic value; it cannot then provide a good measure of the SFR of the galaxy, invalidating relations derived from lower SFR systems. This hidden population may also contribute to feedback processes in the galaxies – a factor of 10 more ULXs would boost the radiative feedback by a factor of 10, and a similar level of mechanical feedback would also be expected for these systems. Given that the numbers of massive star-forming systems similar to LIRGs increase to peak at redshifts $\sim$1, this implies that understanding the concealment of X-ray source populations is important for understanding the intrinsic X-ray emission of the galaxies now being picked up in deep surveys, and how the sources that contribute to this emission help shape their host galaxies. Further work that builds on this study and permits a deeper understanding the X-ray populations of nearby LIRGs is therefore key to understanding our X-ray view of galaxies at the peak of cosmic SF.

ACKNOWLEDGEMENTS

We thank the anonymous referee for their suggestions that resulted in improvements to this paper. WL acknowledges support in the form of funding for a PhD studentship from the Royal Thai Fellowship scheme. TPR thanks STFC for support in the form of the standard grant ST/G001588/1 and subsequently as part of the consolidated grant ST/K000861/1. We thank various colleagues for useful conversations, notably Poshak Gandhi for pointing out the CCSNe results and James Mullaney for a helpful discussion in the AGN contribution fitting result. We would also like to thank Steven Willner for a valuable discussion on the effect of dust versus galaxy age.

REFERENCES

Avni Y., 1976, ApJ, 210, 642
Bachetti M. et al., 2013, ApJ, 778, 163
Basu-Zych A. R. et al., 2013a, ApJ, 762, 45
Basu-Zych A. R. et al., 2013b, ApJ, 774, 152
Bedregal A. G., Colina L., Alonso-Herrero A., Arribas S., 2009, ApJ, 698, 1852
Belczynski K., Bulik T., Fryer C. L., Ruiter A., Valsecchi F., Vink J. S., Hurley J. R., 2010, ApJ, 714, 1217
Berghea C. T., Weaver K. A., Colbert E. J. M., Roberts T. P., 2008, ApJ, 687, 471
Broos P. S., Townsley L. K., Feigelson E. D., Getman K. V., Bauer F. E., Garmire G. P., 2010, ApJ, 714, 1582
Broos P., Townsley L., Getman K., Bauer F., 2012, Astrophysics Source Code Library, record ascl:1203.001
Brorby M., Kaaret P., Prestwich A., 2014, MNRAS, 441, 2346
Calzetti D. et al., 2007, ApJ, 666, 870
Calzetti D. et al., 2010, ApJ, 714, 1256
Cash W., 1979, ApJ, 228, 939
Clemens M. S., Scaife A., Vega O., Bressan A., 2010, MNRAS, 405, 887
Colbert E. J. M., Mushotzky R. F., 1999, ApJ, 519, 89
Colbert E. J. M., Heckman T. M., Ptak A. F., Strickland D. K., Weaver K. A., 2004, ApJ, 602, 231
de Vaucouleurs G., de Vaucouleurs A., Corwin H. G., Jr Buta R. J., Paturel G., Fouqué P., 1991, Third Reference Catalogue of Bright Galaxies. Volume I: Explanations and references. Volume II: Data for galaxies between 0^h and 12^h. Volume III: Data for galaxies between 12^h and 24^h. Springer-Verlag, Berlin
Dotan C., Shaviv N. J., 2011, MNRAS, 413, 1623
Fabbiano G., 2006, ARA&A, 44, 323
Fabbiano G., Zezas A., Murray S. S., 2001, ApJ, 554, 1035
Fabian A. C., 2012, ARA&A, 50, 455
Farrell S. A., Webb N. A., Barret D., Godet O., Rodrigues J. M., 2009, Nature, 460, 73
Feng H., Kaaret P., 2007, ApJ, 668, 941
Feng H., Soria R., 2011, New Astron. Rev., 55, 166
Fragos T. et al., 2013a, ApJ, 764, 41
Fragos T., Lehmer B. D., Naoz S., Zezas A., Basu-Zych A., 2013b, ApJ, 776, L31
Franceschini A. et al., 2003, MNRAS, 343, 1181
Gao Y., Wang Q. D., Appleton P. N., Lucas R. A., 2003, ApJ, 596, L171
Genzel R. et al., 1998, ApJ, 498, 579
Georgakakis A., Nandra K., Laird E. S., Aird J., Trichas M., 2008, MNRAS, 388, 1205
Gladstone J. C., Roberts T. P., 2009, MNRAS, 397, 124
Gladstone J. C., Roberts T. P., Done C., 2009, MNRAS, 397, 1836
Goldader J. D., Joseph R. D., Doyon R., Sanders D. B., 1997, ApJ, 474, 104
González-Alfonso E. et al., 2012, A&A, 541, A4
González-Martín O., Masegosa J., Márquez I., Guerrero M. A., Dultzin-Hacyan D., 2006, A&A, 460, 45
Gonçalves A. C., Soria R., 2006, MNRAS, 371, 673
Grier C. J., Mathur S., Ghosh H., Ferrarese L., 2011, ApJ, 731, 60
Grimm H.-J., Gilfanov M., Sunyaev R., 2003, MNRAS, 339, 793
Grisé F., Pakull M. W., Soria R., Motch C., Smith I. A., Ryder S. D., Böttcher M., 2008, A&A, 486, 151
Grisé F., Kaaret P., Pakull M. W., Motch C., 2011, ApJ, 734, 23
Gültekin K., Cackett E. M., Miller J. M., Di Matteo T., Markoff S., Richstone D. O., 2009, ApJ, 706, 404
Güver T., Özel F., 2009, MNRAS, 400, 2050
Horiuchi S., Beacom J. F., Kochanek C. S., Prieto J. L., Stanek K. Z., Thompson T. A., 2011, ApJ, 738, 154
Huang Z. P., Condon J. J., Yin Q. F., Thuan T. X., 1990, IAU Circ., 4988, 1
Huo Z. Y., Xia X. Y., Xue S. J., Mao S., Deng Z. G., 2004, ApJ, 611, 208
Jenkins L. P., Roberts T. P., Ward M. J., Zezas A., 2004, MNRAS, 352, 1335
Johnson H. L., Morgan W. W., 1953, ApJ, 117, 313
Kaaret P., Alonso-Herrero A., 2008, ApJ, 682, 1020
Kajava J. J. E., Poutanen J., 2009, MNRAS, 398, 1450
Kajava J. J. E., Poutanen J., Farrell S. A., Grisé F., Kaaret P., 2012, MNRAS, 422, 990
Kawashima T., Ohsuga K., Mineshige S., Yoshida T., Heinzeller D., Matsumoto R., 2012, ApJ, 752, 18
King A. R., 2004, MNRAS, 347, L18
Kroupa P., 2001, MNRAS, 322, 231
Lehmer B. D., Alexander D. M., Bauer F. E., Brandt W. N., Goulding A. D., Jenkins L. P., Ptak A., Roberts T. P., 2010, ApJ, 724, 559
Lehmer B. D. et al., 2013, ApJ, 771, 134
Linden T., Kalogera V., Sepinsky J. F., Prestwich A., Zezas A., Gallagher J. S., 2010, ApJ, 725, 1984
Mapelli M., Bressan A., 2013, MNRAS, 430, 3120
Mapelli M., Ripamonti E., Zampieri L., Colpi M., Bressan A., 2010, MNRAS, 408, 234
Mapelli M., Ripamonti E., Zampieri L., Colpi M., 2011, Astron. Nachr., 332, 414
Mattila S. et al., 2012, ApJ, 756, 111
Middleton M. J., Roberts T. P., Done C., Jackson F. E., 2011a, MNRAS, 411, 644
Middleton M. J., Sutton A. D., Roberts T. P., 2011b, MNRAS, 417, 464
Middleton M. J., Walton D. J., Roberts T. P., Heil L., 2014a, MNRAS, 438, L51
Middleton M. J., Heil L., Pintore F., Walton D. J., Roberts T. P., 2014b, MNRAS, submitted
Miller J. M., Walton D. J., King A. L., Reynolds M. T., Fabian A. C., Miller M. C., Reis R. C., 2013, ApJ, 776, L36
Mineo S., Gilfanov M., Sunyaev R., 2012a, MNRAS, 419, 2095

Mineo S., Gilfanov M., Sunyaev R., 2012b, MNRAS, 426, 1870
Mineo S., Rappaport S., Steinhorn B., Levine A., Gilfanov M., Pooley D., 2013, ApJ, 771, 133
Mirabel I. F., Sanders D. B., 1988, ApJ, 335, 104
Mitsuda K. et al., 1984, PASJ, 36, 741
Moustakas J., Kennicutt R. C., Jr, Tremonti C. A., Dale D. A., Smith J.-D. T., Calzetti D., 2010, ApJS, 190, 233
Mullaney J. R., Alexander D. M., Goulding A. D., Hickox R. C., 2011, MNRAS, 414, 1082
Neff S. G., Ulvestad J. S., Teng S. H., 2004, ApJ, 611, 186
Nelemans G., Voss R., Nielsen M. T. B., Roelofs G., 2010, MNRAS, 405, L71
Peterson K. C., Gallagher S. C., Hornschemeier A. E., Muno M. P., Bullard E. C., 2006, AJ, 131, 133
Pietsch W. et al., 2001, A&A, 365, L174
Plotkin R. M., Gallo E., Miller B. P., Baldassare V. F., Treu T., Woo J.-H., 2014, ApJ, 780, 6
Poutanen J., Lipunova G., Fabrika S., Butkevich A. G., Abolmasov P., 2007, MNRAS, 377, 1187
Prestwich A. H., Tsantaki M., Zezas A., Jackson F., Roberts T. P., Foltz R., Linden T., Kalogera V., 2013, ApJ, 769, 92
Ptak A., Colbert E., van der Marel R. P., Roye E., Heckman T., Towne B., 2006, ApJS, 166, 154
Relaño M., Lisenfeld U., Pérez-González P. G., Vílchez J. M., Battaner E., 2007, ApJ, 667, L141
Risaliti G., Elvis M., Fabbiano G., Baldi A., Zezas A., 2005, ApJ, 623, L93
Roberts T. P., 2007, Ap&SS, 311, 203
Sanders D. B., Mazzarella J. M., Kim D.-C., Surace J. A., Soifer B. T., 2003, AJ, 126, 1607
Smith D. A., Wilson A. S., 2003, ApJ, 591, 138
Smith B. J., Swartz D. A., Miller O., Burleson J. A., Nowak M. A., Struck C., 2012, AJ, 143, 144
Soria R., Baldi A., Risaliti G., Fabbiano G., King A., La Parola V., Zezas A., 2007, MNRAS, 379, 1313
Stobbart A.-M., Roberts T. P., Wilms J., 2006, MNRAS, 368, 397
Strateva I. V., Komossa S., 2009, ApJ, 692, 443
Sutton A. D., Roberts T. P., Walton D. J., Gladstone J. C., Scott A. E., 2012, MNRAS, 423, 1154
Sutton A. D., Roberts T. P., Gladstone J. C., Farrell S. A., Reilly E., Goad M. R., Gehrels N., 2013a, MNRAS, 434, 1702
Sutton A. D., Roberts T. P., Middleton M. J., 2013b, MNRAS, 435, 1758
Swartz D. A., Ghosh K. K., Tennant A. F., Wu K., 2004, ApJS, 154, 519
Swartz D. A., Soria R., Tennant A. F., 2008, ApJ, 684, 282
Swartz D. A., Tennant A. F., Soria R., 2009, ApJ, 703, 159
Swartz D. A., Soria R., Tennant A. F., Yukita M., 2011, ApJ, 741, 49
Takagi T., Arimoto N., Vansevičius V., 1999, ApJ, 523, 107
Ulvestad J. S., 2009, AJ, 138, 1529
Vega O., Clemens M. S., Bressan A., Granato G. L., Silva L., Panuzzo P., 2008, A&A, 484, 631
Voss R., Gilfanov M., 2006, A&A, 447, 71
Walton D. J., Roberts T. P., Mateos S., Heard V., 2011, MNRAS, 416, 1844
Walton D. J., Miller J. M., Reis R. C., Fabian A. C., 2012, MNRAS, 426, 473
Walton D. J., Miller J. M., Harrison F. A., Fabian A. C., Roberts T. P., Middleton M. J., Reis R. C., 2013, ApJ, 773, L9
Wang J., Fabbiano G., Elvis M., Risaliti G., Mazzarella J. M., Howell J. H., Lord S., 2009, ApJ, 694, 718
Wilms J., Allen A., McCray R., 2000, ApJ, 542, 914
Windhorst R. A. et al., 1991, ApJ, 380, 362
Yoshida T., Ebisawa K., Matsushita K., Tsujimoto M., Kawaguchi T., 2010, ApJ, 722, 760
Zampieri L., Roberts T. P., 2009, MNRAS, 400, 677
Zaritsky D., Kennicutt R. C., Jr, Huchra J. P., 1994, ApJ, 420, 87
Zezas A., Ward M. J., Murray S. S., 2003, ApJ, 594, L31
Zombeck M. V., 1990, Handbook of the Space Astronomy and Astrophysics, 2nd edn. Cambridge Univ. Press, Worcester

APPENDIX A: A CATALOGUE OF POINT SOURCES DETECTED IN THE LIRG SAMPLE

Here, we present the catalogue of all X-ray point source detections in the *Chandra* observations of our sample of 17 LIRGs. For convenience, we have divided the sources into two tables: the ULX catalogue (sources with $L_X \geq 10^{39}$ erg s^{-1}, Table A1); and the catalogue of less luminous X-ray point sources (Table A2).

Table A1. ULX candidates.

RA	Dec.	Host galaxy	Net counts	Flux (10^{-14} erg cm^{-2} s^{-1})	Luminosity (10^{39} erg s^{-1})	Notes
(1)	(2)	(3)	(4)	(5)	(6)	(7)
00 09 53	+ 25 55 48	NGC 23	$6.62^{+3.78}_{-2.58}$	$0.27^{+0.16}_{-0.11}$	$1.20^{+0.68}_{-0.47}$	
00 09 53	+ 25 55 39	NGC 23	$10.66^{+4.43}_{-3.26}$	$0.44^{+0.18}_{-0.13}$	$1.93^{+0.80}_{-0.59}$	
02 09 38	− 10 08 47	NGC 838	$10.27^{+4.43}_{-3.26}$	$0.58^{+0.25}_{-0.19}$	$1.80^{+0.78}_{-0.57}$	
02 09 39	− 10 08 44	NGC 838	$11.83^{+4.57}_{-3.41}$	$0.67^{+0.26}_{-0.19}$	$2.08^{+0.80}_{-0.60}$	
02 42 38	− 00 01 18	NGC 1068	$385.72^{+20.72}_{-19.69}$	$6.44^{+0.35}_{-0.33}$	$1.46^{+0.08}_{-0.07}$	
02 42 39	− 00 00 55	NGC 1068	$1370.25^{+38.09}_{-37.08}$	$22.87^{+0.64}_{-0.62}$	5.17 ± 0.14	1
02 42 40	− 00 01 01	NGC 1068	$487.09^{+23.84}_{-22.81}$	$8.13^{+0.40}_{-0.38}$	1.84 ± 0.09	
03 33 32	− 36 08 09	NGC 1365	$68.79^{+9.35}_{-8.28}$	$4.02^{+0.55}_{-0.48}$	$1.57^{+0.21}_{-0.19}$	
03 33 34	− 36 11 03	NGC 1365	$123.75^{+12.17}_{-11.12}$	$7.24^{+0.71}_{-0.65}$	$2.82^{+0.28}_{-0.25}$	
03 33 35	− 36 09 37	NGC 1365	$204.89^{+15.34}_{-14.30}$	$11.99^{+0.90}_{-0.84}$	$4.66^{+0.35}_{-0.33}$	
03 33 38	− 36 09 35	NGC 1365	$111.89^{+11.62}_{-10.57}$	$6.55^{+0.68}_{-0.62}$	$2.55^{+0.26}_{-0.24}$	
03 33 40	− 36 07 27	NGC 1365	$68.83^{+9.35}_{-8.28}$	$4.03^{+0.55}_{-0.48}$	$1.57^{+0.21}_{-0.19}$	
03 33 50	− 36 10 26	NGC 1365	$32.88^{+6.81}_{-5.71}$	$2.80^{+0.58}_{-0.49}$	$1.09^{+0.23}_{-0.19}$	
10 22 20	+ 21 34 02	NGC 3221	$16.61^{+5.21}_{-4.08}$	$0.69^{+0.22}_{-0.17}$	$2.91^{+0.91}_{-0.71}$	
10 22 20	+ 21 33 29	NGC 3221	$14.82^{+4.97}_{-3.83}$	$0.61^{+0.21}_{-0.16}$	$2.60^{+0.87}_{-0.67}$	
10 22 20	+ 21 34 50	NGC 3221	$16.74^{+5.21}_{-4.08}$	$0.69^{+0.22}_{-0.17}$	$2.93^{+0.91}_{-0.71}$	

Table A1 – *continued*

RA	Dec.	Host galaxy	Net counts	Flux (10^{-14} erg cm^{-2} s^{-1})	Luminosity (10^{39} erg s^{-1})	Notes
(1)	(2)	(3)	(4)	(5)	(6)	(7)
10 22 20	+ 21 34 05	NGC 3221	$6.63^{+3.78}_{-2.58}$	$0.27^{+0.16}_{-0.11}$	$1.16^{+0.66}_{-0.45}$	
10 22 21	+ 21 33 36	NGC 3221	$14.73^{+4.97}_{-3.83}$	$0.61^{+0.21}_{-0.16}$	$2.58^{+0.87}_{-0.67}$	
10 22 22	+ 21 33 25	NGC 3221	$14.87^{+4.97}_{-3.83}$	$0.62^{+0.21}_{-0.16}$	$2.61^{+0.87}_{-0.67}$	
11 28 27	+ 58 34 07	Arp 299	$16.81^{+5.21}_{-4.08}$	$0.80^{+0.25}_{-0.19}$	$2.22^{+0.69}_{-0.54}$	
11 28 31	+ 58 33 45	Arp 299	$62.30^{+9.84}_{-8.77}$	$2.96^{+0.47}_{-0.42}$	$8.24^{+1.30}_{-1.16}$	
11 28 31	+ 58 33 27	Arp 299	$12.03^{+4.71}_{-3.56}$	$0.57^{+0.22}_{-0.17}$	$1.59^{+0.62}_{-0.47}$	
11 28 32	+ 58 33 18	Arp 299	$48.52^{+8.05}_{-6.97}$	$2.30^{+0.38}_{-0.33}$	$6.42^{+1.06}_{-0.92}$	
11 28 33	+ 58 33 37	Arp 299	$28.32^{+6.55}_{-5.45}$	$1.35^{+0.31}_{-0.26}$	$3.74^{+0.87}_{-0.72}$	2
11 28 33	+ 58 34 03	Arp 299	$32.87^{+6.90}_{-5.80}$	$1.56^{+0.33}_{-0.28}$	$4.34^{+0.91}_{-0.77}$	
11 28 34	+ 58 33 41	Arp 299	$28.02^{+6.55}_{-5.45}$	$1.33^{+0.31}_{-0.26}$	$3.70^{+0.87}_{-0.72}$	
11 28 37	+ 58 33 41	Arp 299	$10.84^{+4.43}_{-3.26}$	$0.51^{+0.21}_{-0.15}$	$1.43^{+0.59}_{-0.43}$	
12 14 10	+ 54 31 27	NGC 4194	$25.27^{+6.56}_{-5.46}$	$0.56^{+0.15}_{-0.12}$	$1.11^{+0.29}_{-0.24}$	
13 25 43	− 29 50 06	NGC 5135	$12.57^{+4.71}_{-3.55}$	$0.40^{+0.15}_{-0.11}$	$1.35^{+0.51}_{-0.38}$	
13 25 45	− 29 50 04	NGC 5135	$31.36^{+6.81}_{-5.72}$	$1.01^{+0.22}_{-0.18}$	$3.37^{+0.73}_{-0.62}$	
13 25 45	− 29 50 14	NGC 5135	$20.53^{+5.66}_{-4.54}$	$0.66^{+0.18}_{-0.15}$	$2.21^{+0.61}_{-0.49}$	
13 25 45	− 29 50 12	NGC 5135	$9.64^{+4.28}_{-3.10}$	$0.31^{+0.14}_{-0.10}$	$1.04^{+0.46}_{-0.33}$	
13 25 45	− 29 50 07	NGC 5135	$13.69^{+4.84}_{-3.69}$	$0.44^{+0.16}_{-0.12}$	$1.47^{+0.52}_{-0.40}$	
13 25 48	− 29 49 48	NGC 5135	$27.77^{+6.36}_{-5.26}$	$0.89^{+0.20}_{-0.17}$	$2.99^{+0.68}_{-0.57}$	
13 58 38	+ 37 25 33	NGC 5395	$7.70^{+3.96}_{-2.76}$	$0.39^{+0.20}_{-0.14}$	$1.35^{+0.69}_{-0.48}$	
13 58 38	+ 37 24 41	NGC 5395	$8.80^{+4.12}_{-2.94}$	$0.44^{+0.21}_{-0.15}$	$1.54^{+0.72}_{-0.51}$	
13 58 39	+ 37 25 32	NGC 5395	$13.68^{+4.84}_{-3.69}$	$0.69^{+0.24}_{-0.19}$	$2.40^{+0.85}_{-0.65}$	
13 58 40	+ 37 26 28	NGC 5395	$6.87^{+3.78}_{-2.58}$	$0.34^{+0.19}_{-0.13}$	$1.20^{+0.66}_{-0.45}$	
14 30 11	+ 31 13 00	NGC 5653	$7.54^{+3.96}_{-2.76}$	$0.36^{+0.19}_{-0.13}$	$1.32^{+0.69}_{-0.48}$	
22 16 08	− 36 50 56	IC 5179	$13.61^{+4.84}_{-3.69}$	$0.89^{+0.32}_{-0.24}$	$2.38^{+0.85}_{-0.65}$	
22 16 08	− 36 50 19	IC 5179	$7.85^{+3.96}_{-2.76}$	$0.52^{+0.26}_{-0.18}$	$1.37^{+0.69}_{-0.48}$	
22 16 10	− 36 50 40	IC 5179	$14.30^{+4.97}_{-3.83}$	$0.94^{+0.33}_{-0.25}$	$2.51^{+0.87}_{-0.67}$	
22 16 10	− 36 50 34	IC 5179	$6.43^{+3.78}_{-2.58}$	$0.42^{+0.25}_{-0.17}$	$1.13^{+0.66}_{-0.45}$	
22 16 10	− 36 50 20	IC 5179	$36.62^{+7.14}_{-6.05}$	$2.41^{+0.47}_{-0.40}$	$6.42^{+1.25}_{-1.06}$	
22 16 10	− 36 50 24	IC 5179	$6.57^{+3.78}_{-2.58}$	$0.43^{+0.25}_{-0.17}$	$1.15^{+0.66}_{-0.45}$	
22 16 12	− 36 50 24	IC 5179	$12.83^{+4.71}_{-3.55}$	$0.84^{+0.31}_{-0.23}$	$2.25^{+0.83}_{-0.62}$	
22 16 12	− 36 50 09	IC 5179	$19.81^{+5.56}_{-4.43}$	$1.30^{+0.36}_{-0.29}$	$3.47^{+0.97}_{-0.78}$	
23 16 14	− 42 35 02	NGC 7552	$50.89^{+8.19}_{-7.12}$	$7.87^{+1.27}_{-1.10}$	$4.37^{+0.70}_{-0.61}$	
23 16 16	− 42 35 18	NGC 7552	$11.94^{+4.57}_{-3.41}$	$1.85^{+0.71}_{-0.53}$	$1.03^{+0.39}_{-0.29}$	
23 51 22	+ 20 06 39	NGC 7771	$28.82^{+6.45}_{-5.35}$	$1.35^{+0.30}_{-0.25}$	$5.44^{+1.22}_{-1.01}$	
23 51 24	+ 20 06 38	NGC 7771	$9.67^{+4.28}_{-3.10}$	$0.45^{+0.20}_{-0.15}$	$1.82^{+0.81}_{-0.59}$	
23 51 24	+ 20 06 43	NGC 7771	$18.68^{+5.44}_{-4.32}$	$0.88^{+0.26}_{-0.20}$	$3.53^{+1.03}_{-0.81}$	
23 51 28	+ 20 06 52	NGC 7771	$34.72^{+6.98}_{-5.89}$	$1.63^{+0.33}_{-0.28}$	$6.55^{+1.32}_{-1.11}$	

Notes. The candidate ULX detections, ordered by right ascension (RA). Column 1 and 2: right ascension and declination, at epoch J2000, respectively. Column 3: host galaxy. Column 4: net photon counts. Column 5: source flux. Column 6: source luminosity, assuming the source is at the distance of the host galaxy. Columns 4 – 6 are all quoted from data in the 0.3–10 keV energy band. Column 7: additional notes for the ULXs: (1) CXOU J024238.9-000055 (Smith & Wilson 2003); (2) This ULX is coincident with a radio source detection. This may be related to the ULX; it may be an unrelated radio supernova in the host galaxy; or it might be a background AGN (Ulvestad 2009; Neff, Ulvestad & Teng 2004; Huang et al. 1990).

Table A2. Less luminous X-ray point sources.

RA	Dec.	Host galaxy	Net counts	Flux (10^{-14} erg cm^{-2} s^{-1})	Luminosity (10^{39} erg s^{-1})	Notes
(1)	(2)	(3)	(4)	(5)	(6)	(7)
00 09 53	+ 25 54 55	NGC 23	$3.78^{+3.18}_{-1.91}$	$0.16^{+0.13}_{-0.08}$	$0.68^{+0.57}_{-0.34}$	
00 09 55	+ 25 55 25	NGC 23	$5.29^{+3.60}_{-2.38}$	$0.22^{+0.15}_{-0.10}$	$0.96^{+0.65}_{-0.43}$	
02 09 39	−10 08 38	NGC 838	$4.73^{+3.40}_{-2.15}$	$0.27^{+0.19}_{-0.12}$	$0.83^{+0.60}_{-0.38}$	
02 42 33	−00 01 05	NGC 1068	$58.24^{+8.73}_{-7.66}$	$0.97^{+0.15}_{-0.13}$	0.22 ± 0.03	
02 42 33	−00 01 30	NGC 1068	$4.35^{+3.40}_{-2.15}$	$0.07^{+0.06}_{-0.04}$	0.02 ± 0.01	
02 42 37	+ 00 00 13	NGC 1068	$10.25^{+4.43}_{-3.26}$	$0.17^{+0.07}_{-0.05}$	$0.04^{+0.02}_{-0.01}$	
02 42 37	−00 00 28	NGC 1068	$12.05^{+4.71}_{-3.56}$	$0.20^{+0.08}_{-0.06}$	$0.05^{+0.02}_{-0.01}$	
02 42 37	−00 01 09	NGC 1068	$38.92^{+7.38}_{-6.30}$	$0.65^{+0.12}_{-0.11}$	$0.15^{+0.03}_{-0.02}$	
02 42 37	−00 00 19	NGC 1068	$8.06^{+4.12}_{-2.94}$	$0.13^{+0.07}_{-0.05}$	$0.03^{+0.02}_{-0.01}$	
02 42 38	−00 00 29	NGC 1068	$49.79^{+8.19}_{-7.12}$	$0.83^{+0.14}_{-0.12}$	0.19 ± 0.03	
02 42 38	−00 01 43	NGC 1068	$29.50^{+6.64}_{-5.54}$	$0.49^{+0.11}_{-0.09}$	$0.11^{+0.03}_{-0.02}$	
02 42 38	−00 01 37	NGC 1068	$8.59^{+4.58}_{-3.42}$	$0.14^{+0.08}_{-0.06}$	$0.03^{+0.02}_{-0.01}$	
02 42 39	−00 00 50	NGC 1068	$34.66^{+7.56}_{-6.47}$	$0.58^{+0.13}_{-0.11}$	$0.13^{+0.03}_{-0.02}$	
02 42 39	−00 00 52	NGC 1068	$23.56^{+6.77}_{-5.67}$	$0.39^{+0.11}_{-0.09}$	$0.09^{+0.03}_{-0.02}$	
02 42 39	−00 01 23	NGC 1068	$36.77^{+7.55}_{-6.47}$	$0.61^{+0.13}_{-0.11}$	$0.14^{+0.03}_{-0.02}$	
02 42 39	−00 00 57	NGC 1068	$38.83^{+8.03}_{-6.95}$	$0.65^{+0.13}_{-0.12}$	0.15 ± 0.03	
02 42 39	−00 01 31	NGC 1068	$12.27^{+5.10}_{-3.97}$	$0.20^{+0.09}_{-0.07}$	$0.05^{+0.02}_{-0.01}$	
02 42 39	−00 00 35	NGC 1068	$70.92^{+9.77}_{-8.70}$	$1.18^{+0.16}_{-0.15}$	$0.27^{+0.04}_{-0.03}$	
02 42 39	−00 01 04	NGC 1068	$57.03^{+8.93}_{-7.86}$	$0.95^{+0.15}_{-0.13}$	0.22 ± 0.03	
02 42 40	−00 00 28	NGC 1068	$183.48^{+14.67}_{-13.63}$	$3.06^{+0.24}_{-0.23}$	$0.69^{+0.06}_{-0.05}$	
02 42 40	−00 00 38	NGC 1068	$57.47^{+12.80}_{-11.76}$	$0.96^{+0.21}_{-0.20}$	$0.22^{+0.05}_{-0.04}$	
02 42 41	−00 00 37	NGC 1068	$174.24^{+17.01}_{-15.98}$	$2.91^{+0.28}_{-0.27}$	0.66 ± 0.06	
02 42 41	−00 01 32	NGC 1068	$24.69^{+6.27}_{-5.16}$	$0.41^{+0.10}_{-0.09}$	0.09 ± 0.02	
02 42 41	−00 00 60	NGC 1068	$100.64^{+11.75}_{-10.70}$	$1.68^{+0.20}_{-0.18}$	0.38 ± 0.04	
02 42 41	−00 01 44	NGC 1068	$32.82^{+6.90}_{-5.80}$	$0.55^{+0.12}_{-0.10}$	$0.12^{+0.03}_{-0.02}$	
02 42 41	−00 01 25	NGC 1068	$35.90^{+7.31}_{-6.22}$	$0.60^{+0.12}_{-0.10}$	$0.14^{+0.03}_{-0.02}$	
02 42 41	−00 02 15	NGC 1068	$33.45^{+6.90}_{-5.80}$	$0.56^{+0.12}_{-0.10}$	$0.13^{+0.03}_{-0.02}$	
02 42 41	−00 02 53	NGC 1068	$8.36^{+4.12}_{-2.94}$	$0.14^{+0.07}_{-0.05}$	$0.03^{+0.02}_{-0.01}$	
02 42 42	−00 01 22	NGC 1068	$7.72^{+4.28}_{-3.11}$	$0.13^{+0.07}_{-0.05}$	$0.03^{+0.02}_{-0.01}$	
02 42 42	−00 01 09	NGC 1068	$14.50^{+5.34}_{-4.21}$	$0.24^{+0.09}_{-0.07}$	0.05 ± 0.02	
02 42 42	+ 00 00 02	NGC 1068	$29.16^{+6.73}_{-5.63}$	$0.49^{+0.11}_{-0.09}$	$0.11^{+0.03}_{-0.02}$	
02 42 43	−00 00 52	NGC 1068	$18.12^{+5.67}_{-4.55}$	$0.30^{+0.09}_{-0.08}$	0.07 ± 0.02	
02 42 43	−00 00 48	NGC 1068	$19.87^{+5.88}_{-4.76}$	$0.33^{+0.10}_{-0.08}$	0.08 ± 0.02	
02 42 43	+ 00 00 23	NGC 1068	$10.92^{+4.71}_{-3.56}$	$0.18^{+0.08}_{-0.06}$	$0.04^{+0.02}_{-0.01}$	
02 42 43	−00 00 04	NGC 1068	$10.62^{+5.59}_{-4.47}$	$0.18^{+0.09}_{-0.07}$	0.04 ± 0.02	
02 42 43	−00 02 45	NGC 1068	$60.48^{+8.86}_{-7.79}$	$1.01^{+0.15}_{-0.13}$	0.23 ± 0.03	
02 42 43	−00 01 40	NGC 1068	$110.24^{+11.57}_{-10.52}$	$1.84^{+0.19}_{-0.18}$	0.42 ± 0.04	
02 42 44	−00 00 35	NGC 1068	$95.72^{+10.94}_{-9.88}$	$1.60^{+0.18}_{-0.16}$	0.36 ± 0.04	
02 42 45	−00 00 10	NGC 1068	$61.82^{+8.98}_{-7.91}$	$1.03^{+0.15}_{-0.13}$	0.23 ± 0.03	
02 42 45	−00 01 27	NGC 1068	$7.33^{+3.96}_{-2.76}$	$0.12^{+0.07}_{-0.05}$	0.03 ± 0.01	
02 42 45	−00 02 19	NGC 1068	$51.43^{+8.26}_{-7.19}$	$0.86^{+0.14}_{-0.12}$	0.19 ± 0.03	
02 42 46	−00 00 30	NGC 1068	$29.05^{+6.55}_{-5.45}$	$0.49^{+0.11}_{-0.09}$	0.11 ± 0.02	
02 42 46	+ 00 00 06	NGC 1068	$17.92^{+5.44}_{-4.32}$	$0.30^{+0.09}_{-0.07}$	0.07 ± 0.02	
02 42 47	−00 01 13	NGC 1068	$6.29^{+3.78}_{-2.58}$	$0.11^{+0.06}_{-0.04}$	0.02 ± 0.01	
02 42 47	+ 00 00 28	NGC 1068	$167.85^{+14.03}_{-12.99}$	$2.80^{+0.23}_{-0.22}$	0.63 ± 0.05	
03 33 21	−36 08 15	NGC 1365	$21.48^{+5.77}_{-4.65}$	$1.26^{+0.34}_{-0.27}$	$0.49^{+0.13}_{-0.11}$	
03 33 23	−36 07 53	NGC 1365	$38.58^{+7.31}_{-6.22}$	$2.26^{+0.43}_{-0.36}$	$0.88^{+0.17}_{-0.14}$	
03 33 24	−36 10 50	NGC 1365	$7.42^{+3.96}_{-2.76}$	$0.43^{+0.23}_{-0.16}$	$0.17^{+0.09}_{-0.06}$	
03 33 26	−36 08 38	NGC 1365	$21.74^{+5.77}_{-4.65}$	$1.27^{+0.34}_{-0.27}$	$0.49^{+0.13}_{-0.11}$	

Table A2 – *continued*

RA	Dec.	Host galaxy	Net counts	Flux (10^{-14} erg cm^{-2} s^{-1})	Luminosity (10^{39} erg s^{-1})	Notes
(1)	(2)	(3)	(4)	(5)	(6)	(7)
03 33 26	−36 08 50	NGC 1365	$22.78^{+5.87}_{-4.76}$	$1.33^{+0.34}_{-0.28}$	$0.52^{+0.13}_{-0.11}$	
03 33 27	−36 08 14	NGC 1365	$11.76^{+4.57}_{-3.41}$	$0.69^{+0.27}_{-0.20}$	$0.27^{+0.10}_{-0.08}$	
03 33 30	−36 07 56	NGC 1365	$7.77^{+3.96}_{-2.76}$	$0.45^{+0.23}_{-0.16}$	$0.18^{+0.09}_{-0.06}$	
03 33 30	−36 08 30	NGC 1365	$35.75^{+7.06}_{-5.97}$	$2.09^{+0.41}_{-0.35}$	$0.81^{+0.16}_{-0.14}$	
03 33 30	−36 08 21	NGC 1365	$10.73^{+4.43}_{-3.26}$	$0.63^{+0.26}_{-0.19}$	$0.24^{+0.10}_{-0.07}$	
03 33 31	−36 11 06	NGC 1365	$7.71^{+3.96}_{-2.76}$	$0.45^{+0.23}_{-0.16}$	$0.18^{+0.09}_{-0.06}$	
03 33 31	−36 08 08	NGC 1365	$11.78^{+4.57}_{-3.41}$	$0.69^{+0.27}_{-0.20}$	$0.27^{+0.10}_{-0.08}$	
03 33 32	−36 06 43	NGC 1365	$42.65^{+7.61}_{-6.53}$	$2.50^{+0.45}_{-0.38}$	$0.97^{+0.17}_{-0.15}$	
03 33 32	−36 09 03	NGC 1365	$19.87^{+5.56}_{-4.43}$	$1.16^{+0.32}_{-0.26}$	$0.45^{+0.13}_{-0.10}$	
03 33 33	−36 07 15	NGC 1365	$4.81^{+3.40}_{-2.15}$	$0.28^{+0.20}_{-0.13}$	$0.11^{+0.08}_{-0.05}$	
03 33 36	−36 08 21	NGC 1365	$25.57^{+6.56}_{-5.46}$	$1.50^{+0.38}_{-0.32}$	$0.58^{+0.15}_{-0.12}$	
03 33 36	−36 05 57	NGC 1365	$4.62^{+3.40}_{-2.15}$	$0.27^{+0.20}_{-0.13}$	$0.11^{+0.08}_{-0.05}$	
03 33 36	−36 09 58	NGC 1365	$8.91^{+4.12}_{-2.94}$	$0.52^{+0.24}_{-0.17}$	$0.20^{+0.09}_{-0.07}$	
03 33 37	−36 10 26	NGC 1365	$17.80^{+5.33}_{-4.20}$	$1.04^{+0.31}_{-0.25}$	$0.40^{+0.12}_{-0.10}$	
03 33 39	−36 08 01	NGC 1365	$4.80^{+3.40}_{-2.15}$	$0.28^{+0.20}_{-0.13}$	$0.11^{+0.08}_{-0.05}$	
03 33 39	−36 05 24	NGC 1365	$13.43^{+4.84}_{-3.69}$	$0.79^{+0.28}_{-0.22}$	$0.31^{+0.11}_{-0.08}$	
03 33 39	−36 10 02	NGC 1365	$20.82^{+5.66}_{-4.54}$	$1.22^{+0.33}_{-0.27}$	$0.47^{+0.13}_{-0.10}$	
03 33 40	−36 10 37	NGC 1365	$31.85^{+6.72}_{-5.62}$	$1.86^{+0.39}_{-0.33}$	$0.72^{+0.15}_{-0.13}$	
03 33 42	−36 08 19	NGC 1365	$4.87^{+3.40}_{-2.15}$	$0.29^{+0.20}_{-0.13}$	$0.11^{+0.08}_{-0.05}$	
03 33 42	−36 07 41	NGC 1365	$18.79^{+5.44}_{-4.32}$	$1.10^{+0.32}_{-0.25}$	$0.43^{+0.12}_{-0.10}$	
11 28 34	+ 58 33 24	Arp 299	$6.41^{+3.78}_{-2.58}$	$0.30^{+0.18}_{-0.12}$	$0.85^{+0.50}_{-0.34}$	
12 14 09	+ 54 31 45	NGC 4194	$13.84^{+4.97}_{-3.83}$	$0.31^{+0.11}_{-0.09}$	$0.61^{+0.22}_{-0.17}$	
12 14 10	+ 54 31 42	NGC 4194	$11.61^{+4.57}_{-3.41}$	$0.26^{+0.10}_{-0.08}$	$0.51^{+0.20}_{-0.15}$	
12 14 13	+ 54 31 29	NGC 4194	$5.59^{+3.60}_{-2.38}$	$0.14^{+0.08}_{-0.06}$	$0.27^{+0.17}_{-0.15}$	
12 26 54	−00 52 54	NGC 4418	$7.78^{+3.96}_{-2.76}$	$0.31^{+0.16}_{-0.11}$	$0.38^{+0.20}_{-0.14}$	
13 25 44	−29 49 33	NGC 5135	$7.67^{+3.96}_{-2.76}$	$0.25^{+0.13}_{-0.09}$	$0.82^{+0.43}_{-0.30}$	
13 58 40	+ 37 24 45	NGC 5395	$2.86^{+2.94}_{-1.63}$	$0.14^{+0.15}_{-0.08}$	$0.50^{+0.51}_{-0.29}$	
14 30 10	+ 31 12 33	NGC 5653	$4.80^{+3.40}_{-2.15}$	$0.23^{+0.16}_{-0.10}$	$0.84^{+0.60}_{-0.38}$	
23 16 08	−42 34 36	NGC 7552	$3.93^{+3.18}_{-1.91}$	$0.61^{+0.49}_{-0.30}$	$0.34^{+0.27}_{-0.16}$	
23 16 10	−42 35 08	NGC 7552	$3.92^{+3.18}_{-1.91}$	$0.61^{+0.49}_{-0.30}$	$0.34^{+0.27}_{-0.16}$	
23 16 11	−42 34 43	NGC 7552	$8.82^{+4.12}_{-2.94}$	$1.36^{+0.64}_{-0.45}$	$0.76^{+0.35}_{-0.25}$	
23 16 14	−42 35 40	NGC 7552	$10.95^{+4.43}_{-3.26}$	$1.69^{+0.68}_{-0.50}$	$0.94^{+0.38}_{-0.28}$	
23 16 17	−42 35 00	NGC 7552	$7.93^{+3.96}_{-2.76}$	$1.23^{+0.61}_{-0.43}$	$0.68^{+0.34}_{-0.24}$	
23 51 24	+ 20 06 19	NGC 7771	$2.81^{+2.94}_{-1.63}$	$0.13^{+0.14}_{-0.08}$	$0.53^{+0.55}_{-0.31}$	
23 51 26	+ 20 06 47	NGC 7771	$4.62^{+3.40}_{-2.15}$	$0.22^{+0.16}_{-0.10}$	$0.87^{+0.64}_{-0.41}$	
23 51 26	+ 20 06 55	NGC 7771	$3.64^{+3.18}_{-1.91}$	$0.17^{+0.15}_{-0.09}$	$0.69^{+0.60}_{-0.36}$	
23 51 27	+ 20 06 31	NGC 7771	$4.79^{+3.40}_{-2.15}$	$0.23^{+0.16}_{-0.10}$	$0.90^{+0.64}_{-0.41}$	

Notes. The columns are as per Table A1.

This paper has been typeset from a TEX/LATEX file prepared by the author.